UNIVERSITY OF OKLAHOMA

GRADUATE COLLEGE

HIGH-RESOLUTION XRF-LIDAR SEQUENCE STRATIGRAPHY OF THE LATE GUADALUPIAN CAPITAN SLOPE AT MCKITTRICK CANYON, TEXAS: PROCESS-RESPONSE OF OSCILLATING DELAWARE BASIN SEA LEVEL

A THESIS

SUBMITTED TO THE GRADUATE FACULTY

in partial fulfillment of the requirements for the

Degree of

MASTER OF SCIENCE

By

CHENXI XU
Norman, Oklahoma
2018

HIGH-RESOLUTION XRF-LIDAR SEQUENCE STRATIGRAPHY OF THE LATE GUADALUPIAN CAPITAN SLOPE AT MCKITTRICK CANYON, TEXAS: PROCESS-RESPONSE OF OSCILLATING DELAWARE BASIN SEA LEVEL

A THESIS APPROVED FOR THE
CONOCOPHILLIPS SCHOOL OF GEOLOGY AND GEOPHYSICS

BY

_____
Dr. John D. Pigott, Chair

_____
Dr. Roger M. Slatt

_____
Dr. Kulwadee Pigott

This thesis is dedicated to my father. Although he is no longer physically present in my life, I still feel his impact every day. Without his love and support none of these would be possible.

Acknowledgements

I would like to thank Dr. John D. Pigott for giving me the opportunity to study in OU and conduct researches in the world-famous carbonate outcrops of Permian Basin. I could not have finished this thesis report without your support and guidance. I deeply appreciate your care and patience when I faced trouble during this project. I would like to thank my committee members, Dr. Slatt and Dr. Kulwadee, whose valuable feedback and comments helped me make fast progress. Dr. Slatt inspired me a lot for his editorial assistance. Dr. Kulwadee's talk helped me solve the trouble I met during working on this thesis.

I would also like thank Dr. Hearst in Nation Park for providing me the permit to take this scientific research in Mckittrick Canyon. Also, I need to thank my research group teammates Zhuobo Wang, Travis Moreland, and Sofia Caylor, for their help in collecting massive data and accompany in the Mckittrick Canyon. I could never forget the hard but joyful field time with you. I would also thank Jianjun Li and Jing Zhang for their encouragements and suggestions when I was down. Additionally, I need to thank Rui Zhai for sharing his knowledge. I would like to thank Cy Frazier for his help on my thesis format reviewing.

Finally, my deep and sincere gratitude to my family members Hui Xu and Heng Chen for their endless love, help and support. Without them, I could never have the great change to study in USA.

Table of Contents

Acknowledgements iv

Abstract xii

Chapter 1. Introduction 1

1.1 Problem Statement 1

1.2 Study Location 4

1.3 Previous work 6

Chapter 2: Geologic Setting 8

2.1 Geologic Evolution 8

2.2 Stratigraphy 10

2.3 Facies Model 13

Chapter 3: Methods 15

3.1 Field Work 15

3.2 LiDAR 16

3.2.1 Field Collection Procedure 16

3.2.2 Processing 20

3.2.3 Post Processing 23

3.3 X-Ray Fluorescence 24

3.3.1 Hierarchical Cluster Analysis 25

3.3.2 Lithologic Composition 26

3.3.3 XRF Pseudo Gamma Ray 26

3.3.4 Molybdenum-Uranium Proxies 27

Chapter 4: Observation and Interpretation 29

4.1 Trace Element Proxies 29

4.1.1 Gamma Ray Logs and Pseudo-Gamma Ray Logs 29

4.1.2 Hierarchical Cluster Analysis 34

4.1.3 Siliciclastic-Carbonate Proxies 37

4.1.4 Redox Proxies 43

4.1.5 Paleoredox 47

4.2 Sequence Stratigraphy 51

4.2.1 Reviews and Terminology 51

4.2.2 Lidar Sequence Boundaries 54

4.2.3 Chemostratigraphy 62

4.2.4 Sequence Stratigraphic Frameworks 67

4.2.5 Sequence Depositional Settings 71

4.2.6 Sea Level Variations 74

Chapter 5 Conclusion 77

References 79

List of Tables

Table 1: Simplified Stratigraphic chart for the Guadalupe Mountains (Northwest Shelf) and the equivalent basinal members. Modified from Tinker (1998), Kerans and Kempter(2002), Rush and Kerans (2010). 11

Table 2: Amount of data points before and after the application of Octree Filter. Examples of Scan 7 and Scan 8. 21

Table 3: Geochemical data of post-Archean average shale compositions (Taylor and Mclennan, 1985). The values of X average shale and Al average shale can be read through the table. 28

Table 4: Six major clusters and their associated elements. 36

Table 5: Selected elemental proxies in siliciclastic proxies, carbonate proxies, and redox proxies. 36

Table 6: Redox classification of the depositional environments, by Tyson and Pearson (1991) 47

Table 7: Sequence models and their associated systems tracts. From Pigott et al. (2012). 52

Table 8: Sequence stratigraphic framework of previous work and in this study. 53

Table 9: Characteristics of twelve identified packages in terms of proxy variation. The descriptive term in the interpretation is not an absolute value but a relative descriptive term. 65

Table 10: The start and end times of systems tracts and associated proxy variations in this study. 67

List of Figures

Figure 1:Location map of Delaware Basin and McKittrick Canyon. McKittrick Canyon is highlighted in red dot. Hovey Channel is to the South of Delaware basin highlighted by a green arrow. 4

Figure 2: Location map of McKittrick Canyon. Two measured sections (MCK 1 and MCK 2) outlined in black lines start and end at red points. Image taken from Google Earth. The boundaries between shelf and slope and basin highlighted in color dash lines. 5

Figure 3: The schematic transection of platform to slope to basin. The slope terminologies listed along slope according to their dip angles. 6

Figure 4: Paleogeography during the Late Permian. DB represents the Delaware Basin and MB represents the Midland Basin. HV represents the Hovey Channel. Highlighted in the red dashed line is the approximate border of the Delaware Basin. Highlighted in the blue dashed line is the approximate border of the Midland Basin. Highlighted in the black line is the approximate paleoequator location. Highlighted in the green arrow is the approximate location of Hovey Channel. During the Late Permian, the study area was located in a tropical and subtropical climatic setting near the Equator. It provided a great opportunity for the developments of carbonate shelves on the margins. 10

Figure 5: Depositional environments of the Capitan Reef Complex, Guadalupe Mountains, and study areas highlighted in black square. By Beaubouef et al., 1999. 13

Figure 6: The REIGL® VE-400i 3D terrestrial LiDAR used in this study with Nikon camera attached to the top. The yellow part is the tripod at the bottom. 17

Figure 7: Eleven LiDAR scan positions used in this study highlighted in yellow stars on both south and north wall of McKittrick Canyon. 18

Figure 8: The LiDAR Processing work flow employed in the research. 20

Figure 9: Comparison between raw point clouds and Terrain filter applied point clouds for the same location. Left picture shows raw point clouds with substantial vegetation on top of the outcrop. Right picture shows point clouds after Terrain Filter applied. 22

Figure 10: Schematic of strata terminations of onlap and downlap. When initially horizontal strata terminate progressively against an initial inclined surface or inclined strata terminate updip against a greater inclination, the base-discordant relation is defined as onlap. While when initially inclined strata terminate downdip against an initially horizontal or inclined surface, the base-discordant relation is defined as downlap. Modified by Mitchum (1991). 23

Figure 11: An example of the sector diagram showing lithologic composition at stop 2. 26

Figure 12: Cross-plots of comparison between SGR values and XRF derived SGR (PGR) values in toe-of-slope sections and foreslope sections. 30

Figure 13: Comparison between spectral gamma ray curves and pseudo gamma ray curves in foreslope and toe-of-slope slope sections. The spectral gamma ray curves are highlighted in blue lines and the pseudo spectral gamma ray curves derived from XRF data are highlighted in orange lines. 31

Figure 14: Correlation between pseudo gamma ray logs and lithology logs in toe-of-slope sections. 33

Figure 15: Correlation between pseudo gamma ray logs and lithology logs in foreslope sections. 34

Figure 16: The result of hierarchical cluster analysis. Six major clusters are identified and highlighted in colors. 35

Figure 17: Variation of siliciclastic proxies in toe-of-slope sections. The darker colors represent higher values. 39

Figure 18: Variation of siliciclastic proxies in foreslope sections. The darker colors represent higher values. 40

Figure 19: Variation of carbonate proxies in toe-of-slope sections. The darker colors represent higher values. 42

Figure 20: Variation of carbonate proxies in foreslope sections. The darker colors represent higher values. 43

Figure 21: Variation of redox proxies in toe-of-slope sections. The darker colors represent higher values. 45

Figure 22: Variation of redox proxies in foreslope sections. The darker colors represent higher values..... 46

Figure 23: U (EF) vs Mo (EF) for samples from foreslope sections. It indicates the oxic to suboxic environment. 48

Figure 24: U (EF) vs Mo (EF) for samples from toe-of-slope sections. It indicates the suboxic to anoxic environments. 49

Figure 25: Schematic water circulation in Delaware Basin. 50

Figure 26: Interpretation of stratigraphic units and sequence units with Strata Termination shown in 'True Color' view. The three green squares highlighted the detailed sections shown below. Red arrows represent downlap and yellow arrows represent onlap..... 56

Figure 27: Detailed section in 'Reflectance' view of square A..... 57

Figure 28: Detailed type 1 downlap identification in 'Reflenctance' view of square A. Shown in red arrows..... 57

Figure 29: Detailed type 1 downlap identification in 'True Color' view of square A. Shown in red arrows..... 58

Figure 30: Detailed section in 'Reflectance' view of square B..... 58

Figure 31: Detailed type 2 downlap identification in 'Reflectance' view of square B. Shown in red arrows..... 59

Figure 32: Detailed type 2 downlap identification in 'True Color' view of square B. Shown in red arrows. 59
Figure 33: Detailed section in 'Reflectance' view of square C. 60
Figure 34: Detailed type 1 and type 2 onlap identification in 'Reflectance' view of square C. Shown in yellow arrows. Type 1 onlap are observed in toe-of-slope sections and type 2 onlap are observed in foreslope sections. 60
Figure 35: Detailed type 1 and type 2 onlap identification in 'True Color' view of square C. Shown in yellow arrows. Type 1 onlap are observed in toe-of-slope sections and type 2 onlap are observed in foreslope sections. 61
Figure 36: Chemostratigraphic packages interpretation in toe-of-slope sections. The colors in the Package column represent different identified chemostratigraphic packages. 63
Figure 37: Chemostratigraphic packages interpretation in foreslope sections. The colors in the Package column represent different identified chemostratigraphic packages. 64
Figure 38: Sequence stratigraphy framework of toe-of-slope section. 68
Figure 39: Sequence stratigraphy framework of foreslope sections. 69
Figure 40: Slope developments during LST stage. 73
Figure 41: Slope developments during TST stage. 73
Figure 43: Slope developments during RST stage. 74
Figure 42: Slope developments during HST stage. 74
Figure 44: Changes of 4^{th} and 5^{th} order sea level cycles derived from this research correlated to the global sea level curve for the Permian from Haq and Schutter (2008). Long-term 2^{nd} cycles and short-term 3^{rd} sea level cycles of Haq and Schutter (2008) are shown in left column. The high-resolution 4^{th} and 5^{th} order cycles derived from the pseudo gamma ray logs are shown in right column. 76

Abstract

Owing to their intermediate position within the facies tract, carbonate slopes connecting platforms to the basin floor are continuous subaqueous sensitive sedimentologic recorders of changes in sea level and ocean chemistry. This work integrates a novel outcrop approach combining a 3-D LiDAR model with detailed X-Ray Fluorescence data to analyze 4^{th}- and 5^{th}- order sequences for the classic Late Guadalupian strata of McKittrick Canyon, West Texas. Two detailed outcrop sections along slope sections were systematically investigated. The results show that the stratigraphic sequences of late Guadalupian age were divided into five 4th order sequences and further subdivided into fifteen high-frequency cycle sets and twenty possible 5^{th}-level high-frequency cycles. Depositional settings and paleoenvironments owing to oscillations in sea level show pronounced differences in the study area. Two types of onlap and downlap were observed in 3D LiDAR model. The bedding terminations and boundaries are observed through the digital 3D LiDAR model. A hierarchical cluster analysis of 27 element variations shows six major clusters and then grouped in siliciclastic proxies of Si,Ti, Zr, Al, Si/Ti, K, carbonate proxies of Ca, Sr, and redox proxies of U, Mo, V, Ni and Cu. Twelve chemostratigraphic packages are defined based on the variations of elemental proxies. Enrichment of Mo, U and Mo-U Ratios show the foreslope deposits were mostly deposited under oxic to suboxic conditions while toe-of-slope deposits was mostly deposited under suboxic to anoxic conditions. This is interpreted to be associated with the water mass circulation variations caused by relative sea level changes through the Hovey Channel.

Chapter 1. Introduction

1.1 Problem Statement

Carbonate slopes, which connect platforms to the basin floor, are continuous subaqueous sensitive sedimentologic recorders of changes in sea level and changes in ocean chemistry. They not only are hydrocarbon migration pathways updip and provide conduits of allochthonous material downdip for resource plays, but can serve as important oil and gas reservoirs in their own right. In this research, the study area is focused on the carbonate slope sections of the north wall in McKittrick Canyon in the Guadalupe Mountains, western Texas.

Although substantial investigations (e.g. Hurley, 1989; Brown, 1993; Tinker, 1998; Kerans and Kempter, 2002) have been conducted in McKittrick Canyon, the exposed slope has been less well studied owing to the difficulties of bed tracing and very massive vegetation or soil cover. Besides, no published studies have addressed the high-resolution sequence stratigraphic framework based upon the outcrop measured data. To fill the gaps of studying the carbonate slope with outcrop data, this study is the first to establish high-resolution regional sequence stratigraphic frameworks of 4^{th} and 5^{th} order sequences of the classic Late Guadalupian strata and to interpret the paleoredox conditions during these Guadalupian sea level excursions by employing the novel technology combining LiDAR and hand-held XRF.

The fundamental widely used sequence stratigraphic framework of late Guadalupian strata was completed by Tinker (1998) and Kerans (2002). Although there were successive works that followed, most of these interpretations of sequence stratigraphy

were schematic low-resolution compilations. Resolution was not improved as most data for interpretation of the slope sections were collected from well cores miles away instead of being collected directly at the outcrop owing to the difficulty of obscuring vegetation cover and low image quality. Based on the previous study by a spectral gamma ray petrographic analysis of shelf and slope section of the north wall in Mckittrick Canyon by Zhou (2014), there are three questions which need to be answered. They are:

1. Can higher order high-resolution sequences be recognized using a greater detailed elemental assessment as can be afforded by the XRF?

2.What are the paleooxygen conditions during these Guadalupian sea level excursions? What are the possible causes?

3. What are the paleodepositional settings responsible for different systems tracts?

To solve the above questions, the objectives of this study include: 1) measure and describe lithology, texture, grain components, sediment structure and depositional facies for each measured section; 2) collect XRF data for each measured section; 3) collect LiDAR data and build a 3D digital model of the north wall of McKittrick Canyon; 4) establish high-resolution stratigraphic sequence frameworks 5) interpret the paleo depositional and paleo oxygen environments, and illustrate the depositional settings within different systems tracts.

To achieve the objectivities above, this study integrates a novel outcrop approach combining a 3D LiDAR model with measured sections using detailed X-Ray Fluorescence analyses. LiDAR - the light detection and ranging laser scanner - could solve the problem of accessibilities and make it possible to identify layers along the

canyon in different aspects. In addition, the non-destructive hand-held X-ray fluorescence analyzer provides a detailed elemental composition at each measurement. The variations for those major elements and trace elements are of great importance to study the chemostratigraphy of slope and paleoenvironments at the different geologic stage. Besides, the lithology, texture, grain components and sediment structure is also recorded to reconstruct the depositional history and calibrate the XRF data.

After this study, the regional sequence stratigraphic framework will allow researchers to better predict the stratigraphic condition in basins with the similar depositional environments. The 3D LiDAR model of McKittrick Canyon can be attached to other geologic data such as elastic properties or strength of rock studies. Besides, the high-resolution 3D model can be extraordinarily valuable to Guadalupe Mountains National Park for achieving the visual reality for tourists and researchers.

1.2 Study Location

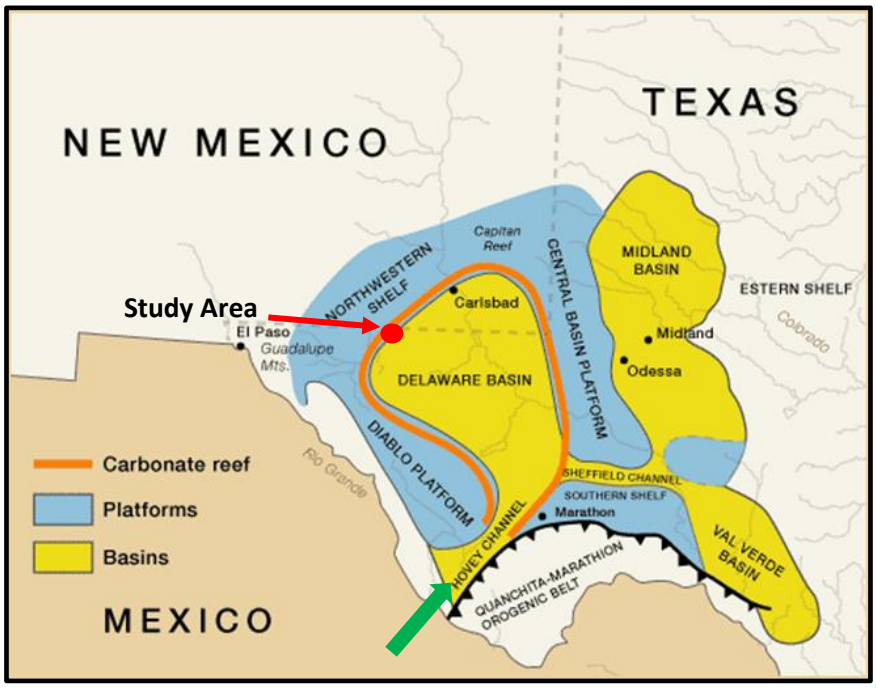

Figure 1:Location map of Delaware Basin and McKittrick Canyon. McKittrick Canyon is highlighted in red dot. Hovey Channel is to the South of Delaware basin highlighted by a green arrow.

The Permian Basin, located in western Texas and southeastern New Mexico, comprises a series of northwest-southeast trending platforms and basins; of these, the Delaware Basin is the second largest basin that is famous for holding large oil fields (Geogory, 2013). At the northwestern border of the Delaware Basin, the Guadalupe Mountain is famous for some of the most spectacular fossilized reef outcrops in the world and geologic research here. The North wall of McKittrick Canyon, where lateral and vertical observation of a complete shelf to basin exposure of Late Guadalupian strata are well exposed, is a good spot to study the slope between the shelf and the basin.

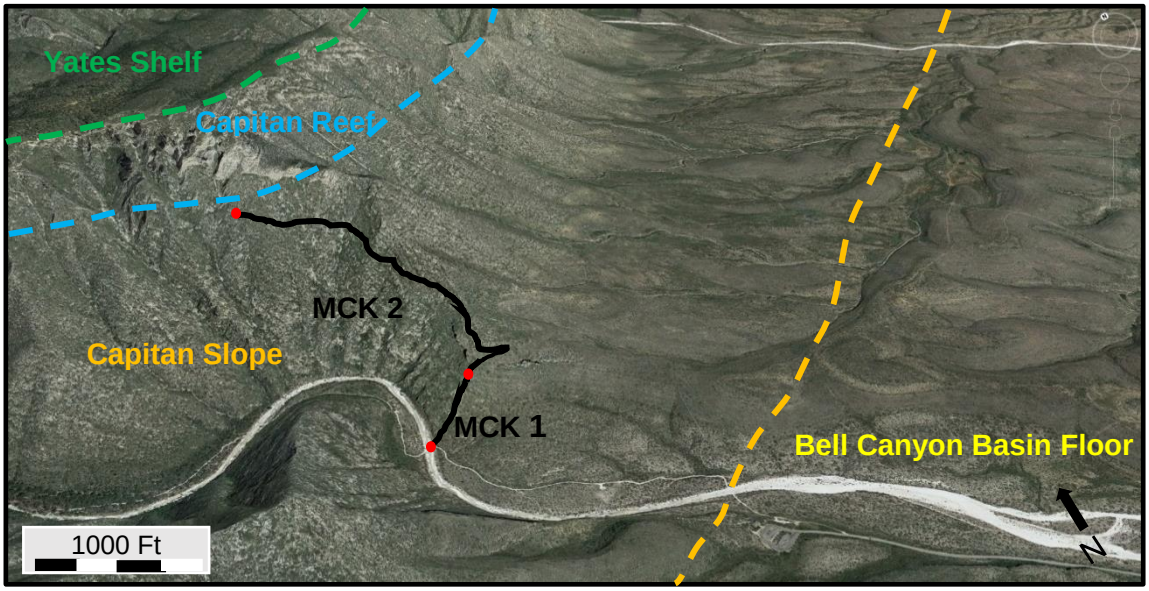

Figure 2: Location map of McKittrick Canyon. Two measured sections (MCK 1 and MCK 2) outlined in black lines start and end at red points. Image taken from Google Earth. The boundaries between shelf and slope and basin highlighted in color dash lines.

Two measure sections were obtained on the north wall in McKittrick Canyon named MCK 1 and MCK 2 (Figure 2). The MCK 1 is measured from Stop 9 to Stop 14 on the Permian Geology Reef Trail. This section covers Yates 6 to Tansill 2 time-equivalent foreslope sections. From the bottom of the intersection between the river creek bed and the sidewalk, the MCK 2 is measured to the Stop 8 of the Permian Geology Reef Trail along Yates 4 to Tansill 1 time-equivalent toe-of-slop sections.

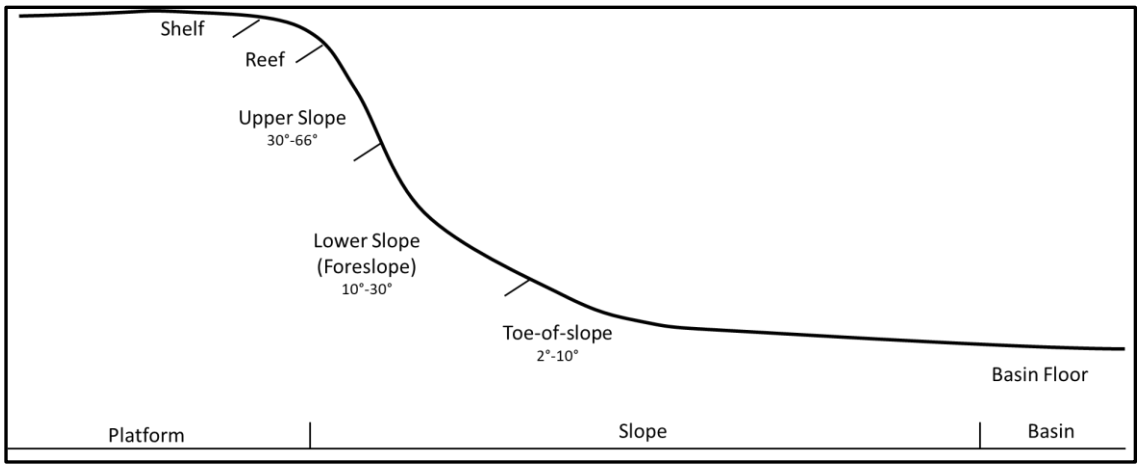

Figure 3: The schematic transection of platform to slope to basin. The slope terminologies listed along slope according to their dip angles.

In this study, the slope sections can be divided into upper slope, medial or fore- slope and lower or toe-of- slope sections (Figure 3). Upper slope refers to the steeply dipping slope with dips ranging between 30 – 66 ° (Playton, 2008). Lower or fore- slope refers to the moderately dipping basin margin with the dip angle between 10° to 30°. Toe-of-slope refers to the gently dipping basin margin with the dip angle between 2° to 10° and usually extend two to four miles into the basin (Cook, 1983).

1.3 Previous work

Shortly after the valuable ideas on stratigraphy by Fielder (1933), the first comprehensive studies combined with a detailed mapping project in Guadalupian Mountains was conducted by King (1942;1948). He established the stratigraphic framework from the deposits of the Delaware basin to the reef margins of northwestern Guadalupian Mountains which is still being used today as the basic stratigraphic reference. Meissner (1972) crafted a depositional model for carbonate sequences on the shelf that was interpreted to respond to sea level variations. Dunham (1972) demonstrated the Permian reef complex in the Guadalupe Mountains to include in a unique mixed

siliciclastic-carbonate environment. Sarg (1988) demonstrated the relative sea level as the most significant feature to determine the carbonate deposition and cyclical changes after reviewing many types of carbonate platforms of Guadalupe Mountains. Bebout (1993) published a guidebook to the Permian Reef Trail and provided the detailed description of the carbonate facies encountered along the Permian Reef Trail with a brief interpretation of depositional environments. Handford (1993) further developed the depositional model and related the depositional settings with different sea level phrases as HSTs, TSTs, and LSTs. Tinker (1998) correlated the shelf-to-basin stratigraphic units for the Capitan depositional system and provided a more complete high-frequency sequence-stratigraphic interpretation. Osleger (1998) detailed the high-frequency sequences of the Yates formation within meter-scale divisions in nearby Slaughter Canyon. Fagerstrom (1999) illustrates the minimal biostratigraph and diagenetic alteration on the Capitan Reef and suggested nearly all fragments of toppled sponges were developed in-situ. Combining this groundwork, Kerans and Kempter (2002) proposed a high-frequency sequence stratigraphic framework for all Guadalupian strata. Playton (2008) later illustrated the facies distribution model of Guadalupian Mountains. Rush and Kerans (2010) documented the depositional architecture of the entire Tansill formation exposed at the carbonate platform in Walnut Canyon. In terms of placing the Guadalupe Mountains into a basin framework, recent works are those by Lew (2013), Williams et al. (2014), Pigott et al. (2014), and Pigott et al. (2016).

Chapter 2: Geologic Setting

2.1 Geologic Evolution

During the Upper Cambrian to Upper Devonian and probable Lower Mississippian, primarily shallow marine carbonate sediment and less extensive siliciclastic sediments were deposited in the Tobosa Basin (Pigott el, al., 2015). During Middle to Late Mississippian time, the Delaware Basin and Midland Basin began to evolve at the same time while a mildly deformed median ridge separated the Tobosa Basin. The ridge later defined the present Central Basin Platform. The platform was established by flexural lithospheric uplift (Pigott et, al., 2016) during 'Collision Phase' caused by the collision between the North and South American continental plates. The Ouachita – Marathon fold belt was then formed, and the Tobosa Basin became structurally modified by the reactivation of high-angle basement faults along pre-existing zones of weakness (Horak, 1985).

During the Pennsylvanian, the region was located approximately 10° south of the Equator. The broad carbonate shelves were well developed and grew along the basin margins (Mazzulo, 1981). Because of the rapid subsidence during this time, predominantly limestone and limited siliciclastic sediments were deposited at extensive deep areas. Siliciclastic supplies were only input from the north and northwest margins. With the increasing growth of the carbonate shelves, the siliciclastic materials were trapped by the massive carbonate banks at the margin and the basin was sedimentologically starved. Moreover, the organisms were preserved by the sustaining basinal sediment compaction and uncirculated water bottoms (Hills, 1984).

During the Early Permian (Wolfcampian), accommodation was created by continuing basin subsidence. Also, the inputs of siliciclastic materials were increasing owing to the rapid rising on the carbonate margins in the northwest, west, and southwest portion (Adams, 1965). But the rate of the development of the carbonate margins was not that rapid and only responsible for the slight restriction of basin circulation with normal marine salinity. In the Late Wolfcampian, thousand-feet carbonate beds replaced the limestones as a result of the decreasing siliciclastic inputs (Hill, 1984).

During the Middle-Permian (Leonardian), both the rate of basinal subsidence and the elevation of the margins increased. The preexisted margins were then becoming more distinctive rimmed margins. The Hovey Channel was the only access to the south and the Panthalassa Ocean. Basinal circulation was severely constricted during this stage. In the Late Leonardian, renewed uplifts on the northwest margin of the Delaware Basin resulted in the increasing siliciclastic input into the basin (Hill, 1984).

During the Late Permian (Guadalupian) (Figure 4), the inactive tectonic movements provided the opportunity for the shallow platforms and deep basins to deposit sands and silts around 3000-4000 ft thickness. The basin subsided owing to the rapid compaction and slow basinal tilting. However, by the end of the Guadalupian, the sedimentation rate in the center was decreasing according to the rapid development of carbonate reefs at the basin margin and the slowing subsidence of the basin (Mazzulo,1981). Therefore, the basin became more restricted.

During the Late Permian (Ochoan), the basinal restriction continued and caused the Castile evaporite to fill in the basin with the thickness around 2000 ft (Hill, 1984). Besides, much subaerial exposure of the Castile evaporites happened and probably

hundreds of feet of Upper Guadalupian formations were removed at the close of the Permian.

During the Mesozoic, the Late Cretaceous compressional Laramide Orogeny began, and the Guadalupe Mountain area was uplifted thousands of feet above the sea level. During the Cenozoic, the Range orogeny began to form the Permian Basin with present-day geographic features.

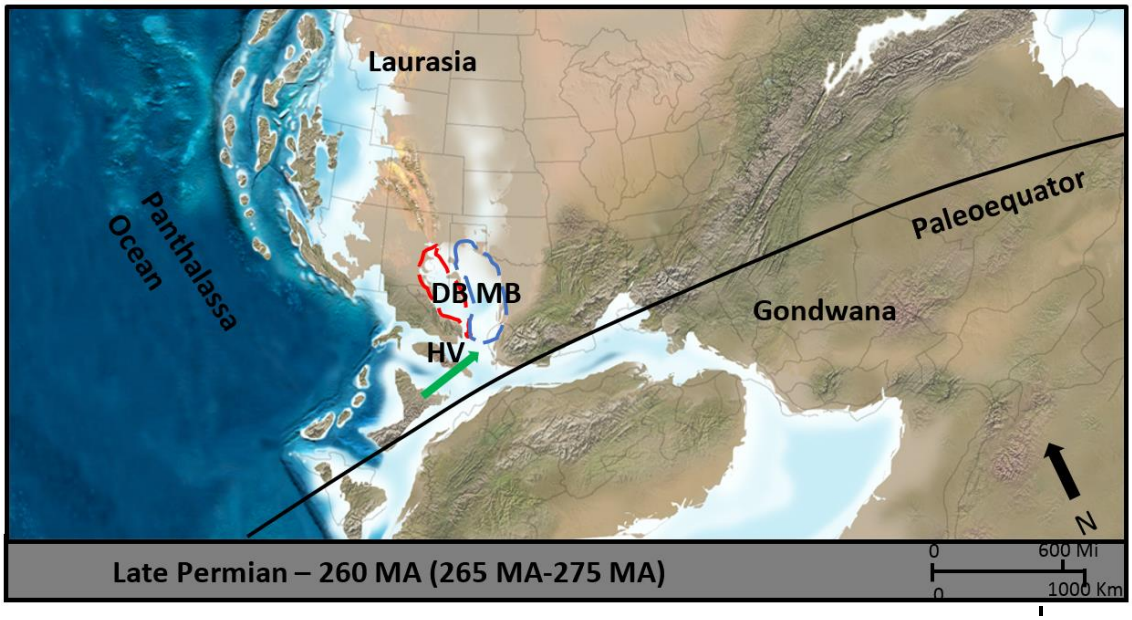

Figure 4: Paleogeography during the Late Permian. DB represents the Delaware Basin and MB represents the Midland Basin. HV represents the Hovey Channel. Highlighted in the red dashed line is the approximate border of the Delaware Basin. Highlighted in the blue dashed line is the approximate border of the Midland Basin. Highlighted in the black line is the approximate paleoequator location. Highlighted in the green arrow is the approximate location of Hovey Channel. During the Late Permian, the study area was located in a tropical and subtropical climatic setting near the Equator. It provided a great opportunity for the developments of carbonate shelves on the margins.

2.2 Stratigraphy

A generalized stratigraphic column of the Delaware Basin is shown in Table 1. During the Late Guadalupian, the Seven River, Yates, and Tansill formations of the

Artesia Group were deposited on the Northwest shelf, whereas the time equivalent Bell Canyon Formation developed as basin deposits. Between the shelf and the basin, the Capitan reef complex was formed on the highly dipping shelf margin (Hill, 1996b).

<table>
<tr><th colspan="3" rowspan="2">AGE</th><th colspan="3">Northwestern Shelf</th><th rowspan="2">Shelf Margin</th><th>Delaware Basin</th></tr>
<tr><th colspan="2">Formations</th><th>Members</th><th>Members and Formations</th></tr>
<tr><td rowspan="11">Permian</td><td rowspan="11">Late Guadalupian</td><td rowspan="3">260.4
Late Capitanian</td><td colspan="2" rowspan="3">Tansill</td><td>Upper Tansill Carbonate</td><td rowspan="11">Capitan Massive</td><td rowspan="2">Post-Lamar Limestone</td></tr>
<tr><td>Ocotillo Silts</td></tr>
<tr><td>Lower Tansill Carbonate</td><td>Lamar Limestone</td></tr>
<tr><td rowspan="4">Middle Capitanian</td><td rowspan="8">Yates</td><td rowspan="3">Yates 6</td><td>Upper Triplet Sand</td><td>Bell Canyon Sand C</td></tr>
<tr><td>Mid Triplet Carbonate</td><td>McKittrick Limestone</td></tr>
<tr><td rowspan="2">Lower Triplet Sand</td><td rowspan="2">Bell Canyon Sand B</td></tr>
<tr><td rowspan="4">Early Capitanian</td></tr>
<tr><td rowspan="2">Yates 5</td><td>Hairpin</td><td>McComb Limestone</td></tr>
<tr><td>Corral</td><td>Bell Canyon Sand A</td></tr>
<tr><td>265.8</td><td>Yates 4</td><td></td><td>Upper Rader Limestone</td></tr>
</table>

Table 1: Simplified Stratigraphic chart for the Guadalupe Mountains (Northwest Shelf) and the equivalent basinal members. Modified from Tinker (1998), Kerans and Kempter(2002), Rush and Kerans (2010).

The Yates formation is characterized by primary gray sand with some beds of carbonate and shales while the Tansill formation consists predominantly of carbonate with thin beds of sands (Hernon, 1953). The Yates formation can be divided into several informal members referred to as Triplet, Hairpin, Corral, and Primitive. In addition, the

Triplet is subdivided into three units: lower Triplet sandstone, Triplet Carbonate, and upper Triplet sandstone (Esteban, 1977).

The Tansill formation is the youngest shelf former of the Artesia Group and further divided into a carbonate-dominated interval analogous to the lower Tansill carbonate, the Ocotillo siltstone, and the topmost upper Tansill carbonates. The Capitan formation is characterized by thick-bedded, coarse, basinward-dipping, massive slope deposits and white unbedded limestones of reef facies. Furthermore, the Capitan Reef is divided into three parts: lower Capitan, middle Capitan, and upper Capitan, and which consists of transgressive and highstand catch-up and keep-up reefs (Kerans, 1997). In the Basin, the Bell Canyon is the uppermost formation of the Guadalupe series and has a lower contact with the Cherry Canyon formation. It is composed of sandstone wedges and less frequent limestone tongues at the toe-of-slope section and thickly bedded carbonates with thin limestone and hard shale beds in the basin (King,1948). In the high-frequency sequence stratigraphic framework established by Tinker (1998), the Yates is subdivided into six high-frequency sequences (Y1-Y6) and Tansill is subdivided into two high-frequency sequences (T1-T2).

2.3 Facies Model

The facies model in Figure 5, that shows the profile of shelf to slope to basin of the North West shelf of the Delaware Basin, is based on Beaubouef's (1999) synthesis of previous works. Within this model, Playton (2008) interpreted the foreslopes to have formed in the Delaware Basin during the late Guadalupian as a debris-dominated foreslope system. At the foreslope sections, the debris-derived complexes are composed by small-scale collapses, the accretion of upgrowing reefs, or of topographically low areas refilling by coarse-grained, matrix poor sediments. Playton (2008) suggested dominant deposits at the toe-of-slope sections are thin-bedded calciturbidites and shales and fine-grained sandstone to siltstone.

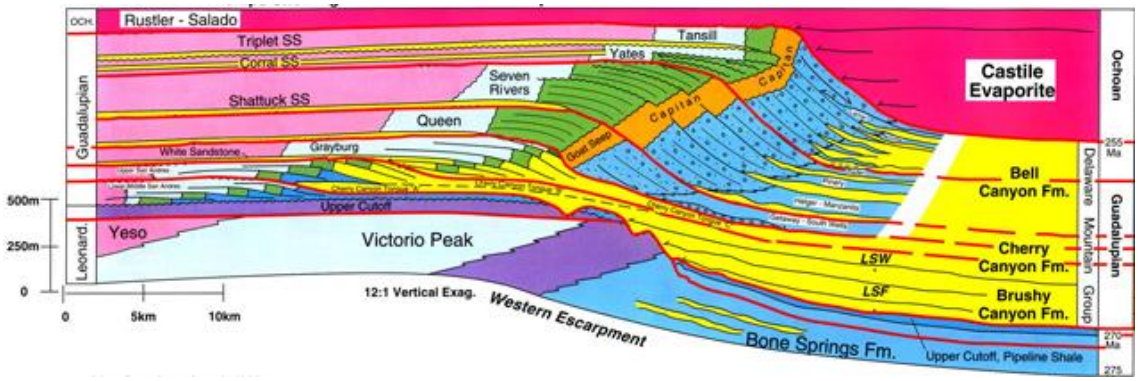

Figure 5: Depositional environments of the Capitan Reef Complex, Guadalupe Mountains, and study areas highlighted in black square. By Beaubouef et al., 1999.

In the mixed siliciclastic-carbonate carbonate shelf, the depositional inputs have a significant relation with the relative sea level. Sangiorgi (2008) propsed that during lowstands, the siliciclastic components (laminated silts and very fine sands) was contributed by eolian deposits caused by dust storms. Furthermore, some terrigenous

sands could also accumulate at the foreslope by bypassing the reef barriers during relative highstands. Brown (1993) proposed that the carbonate muds originated from the carbonate factory on the shelf margin. When the shelf margin is subaerually exposed during relative lowstands, the carbonate muds will sharply be reduced to almost none. Instead, the carbonate muds can only be deposited when the shelf was flooded during relative high sea level. But rapid sea-level rise may also reduce the production of carbonate muds by drowning those reefs with relative low catch-up growing rates.

Chapter 3: Methods

3.1 Field Work

The field work contained mainly two parts, LiDAR data collection and detailed field observation on XRF measured sections. All the field work was conducted between the spring of 2016 and the spring of 2017. Owing to the intensive workload for LiDAR and remote measured sections, six field trips of five to seven days each were required to complete the field data collection work.

LiDAR scan positions were selected on both sides of Mckittrick Canyon to reduce the generation of LiDAR shadow (Figure 7). Details will be discussed in the following Chapter 3.2.

Field observations were taken at two different outcrop locations (MCK 1 And MCK 2) at the north wall of Mckittrick canyon. These two measured sections could nearly combine all the slope section of McKittrick Canyon. MCK 1 is located to extend across the whole toe-of-slope section, which is from the intersection of the sidewalk and the creek bed to the first switch point at stop 8 on the Permian Reef Trail. Roughly five foot intervals were selected for MCK 1 as sample distances. MCK 2 is located from the first switch point at stop 8 to the second switch point at stop 14 along the Permian Reef Trail. The detailed geologic descriptions along the trail were available in Mruk and Bebout (1993). Because the very thick stratification and undulations of the elevations along the trail, sample distance was selected approximately one-hundred foot to reconcile the stratigraphic variations observed cross the foreslope.

At the two measured sections, observations were taken including lithologies, textures, grain components and sediment structures. The hand-held XRF collects the data either directly from the fresh surface on in-situ outcrops or rock pieces knocked by the rock hammer. Outcrop photos were taken by iPhone 6s and GPS locations were recorded by a Garmin Montana 650t at each position.

3.2 LiDAR

3.2.1 Field Collection Procedure

LiDAR (light and detection ranging) has been widely used among a large variety of fields including scientific, surveying and construction application. For example, Oskin (2012) detected previously undocumented blind faults within thick sediments of the Colorado River delta after comparing LiDAR data before and after an earthquake. Lefsky (2008) used LiDAR to image the above-ground biomass in three biomes. For geological application, the LiDAR has been also used to image field outcrops and generate 3D models. With the help of LiDAR, Pringle (2004) built virtual outcrop models of the Carboniferous Shale Grit Formation at Alport Castles, Derbyshire, UK. Buckley (2010) mapped the geological features and correlated the layers between multiple outcrop facies in the Ivie Creek area, Utah. Garrett (2016) built the 3D LiDAR model for the eastern wall in Slaughter Canyon with the same instrument used in this study.

Figure 6: The REIGL® VE-400i 3D terrestrial LiDAR used in this study with Nikon camera attached to the top. The yellow part is the tripod at the bottom.

The LiDAR used in this research is a REIGL® VE-400i 3D terrestrial laser scanner (Figure 6) with a one-thousand-meter maximum range. A laser pulse is emitted from the beam exit window towards outcrops hitting one or several targets, causing one or several echo pulses. Then the pulses are reflected from the targets and received and transformed into electrical signals recorded inside the LiDAR. The LiDAR rotates 360°at a first single scan to fully cover the surrounding areas and the scan time is dependent on the chosen resolution. The GPS locations are also recorded within the inside integrated GPS receiver and scanner's own coordinate system (SOCS) is later established at each scan position.

In order to minimize acquisition shadows in Mckittrick Canyon, scan positions were firstly determined on Google Maps and then tested and altered individually in the field. Seventeen scan positions were selected in the actual operation in the field and eleven scan positions were finally employed in this research (Figure 7). Among them, three (ScanPos #8; ScanPos #10; ScanPos #1) were taken to the South of the canyon creek bed, five (ScanPos #2; ScanPos #3; ScanPos #6; ScanPos #7; ScanPos #17) were taken to the north part of canyon creek bed, two (ScanPos #12; ScanPos #13) were taken on the mountainside of the south wall and two (ScanPos #15, ScanPos #16) were taken taken along the Permian Reef Trail.

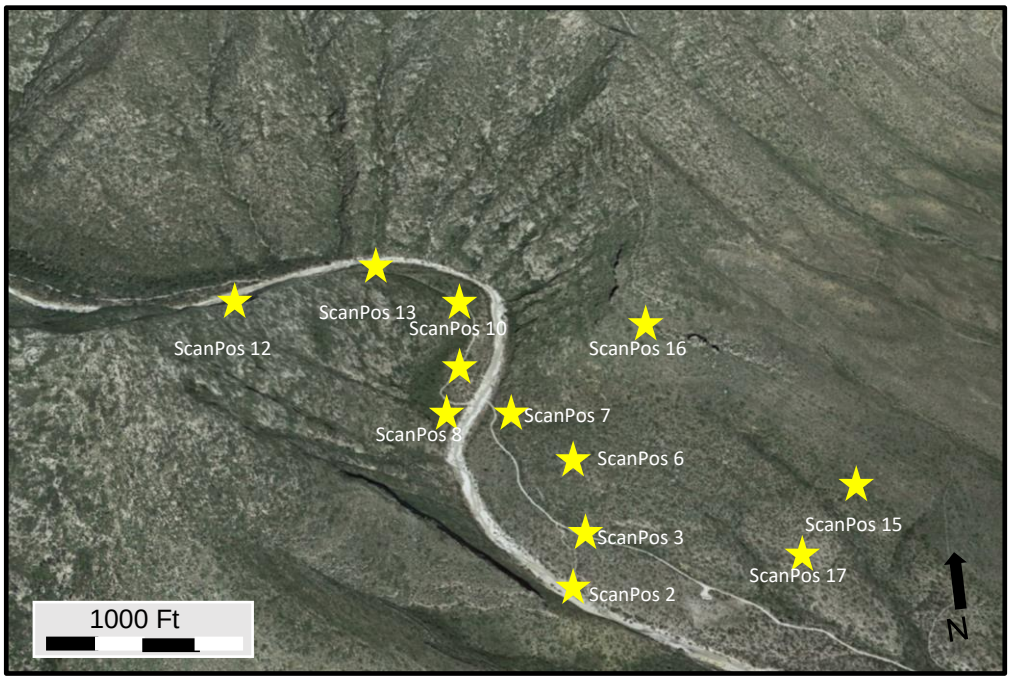

Figure 7: Eleven LiDAR scan positions used in this study highlighted in yellow stars on both south and north wall of McKittrick Canyon.

The collection process includes preparation before scanning and the LiDAR operation. To combine scans together with the proper spatial relations, highly reflective objects (targets) are required to be placed on the outcrops between scan positions. At least

three of the highly reflective objects should be identified between adjacent scans. Whether the highly reflective objects could be efficiently identified depends largely on their orientation to each scan position and the impedance of vegetation or other rocks between objects and the LiDAR instrument. The highly reflective objects are 5cm flat round reflectors and 10 cm high cylinders. Flat reflectors are placed on the flat surfaces and top of stable vegetation, while cylinders are placed at extensively visible areas with the deep angle and wide-open areas. Reflectors and cylinders should be retrieved after all scans where finished.

After reflectors and cylinders are all positioned, the LiDAR is fastened to a tripod on relatively flat ground and attached is a Nikon 810 cameral. The LiDAR is then connected to the laptop and external batteries. The Rescan 2.5 software is implemented on the laptop to control the start and end of the process of laser emitting and laser detection at each scan position in real time. At each scan position, a 360° scan is first taken with a resolution of 0.01° for a run time estimated of 62 minutes. For this scan, the Long Range and accurate pose estimation working mode are selected. The scanner records the GPS location and the scan commences. After the 360° scan finishes, the camera rotates 360° to take seven photos with a 20% overlap with each other. The 5cm reflectors and 10 cm cylinders are then identified and registered in the Riscan software while zooming in. The LiDAR then scans again in order to obtain the accurate position of those registered objects.

Once three or more highly reflective objects are successfully identified by the LiDAR, the number of fine scans is determined upon different locations. Fine scans could provide detailed data with higher resolution and less time needed for selected small areas.

Resolutions between 0.002° to 0.004° are used in this research, which translates to one-centimeter resolution. Once fine scans are satisfied enough, the LiDAR is turned off and moved to the next scan position. The same process is repeated at the next position until all scans are conducted.

3.2.2 Processing

After the collection of all the LiDAR data, the processing work was completed by Rescan software in the laboratory. The original stored data format is represented as point clouds and the size for each scan varies from 800 MB to 3 GB. The data allow accessing both in 2D view and 3D view. In 3D views, the common view types used in this research are amplitude, reflectance, and true color. Amplitude is defined as the amplitude of the echo signal reaching the laser scanner (RIEGL, 2013) and the quality is related to a range of the target. Reflectance is defined as wavelength related incident optical power fraction, whose value is dependent on the angle and the range of the target. In true color view type, the color for each point is derived from the high-quality images taken by the Nikon 80D camera. Importantly, the daytime light also affects the image colors.

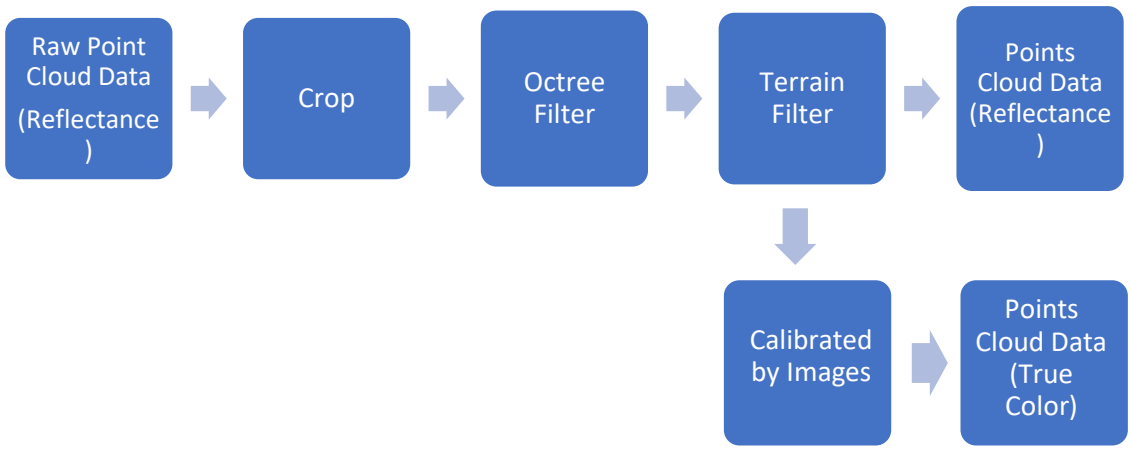

Figure 8: The LiDAR Processing work flow employed in the research.

To eliminate those messy points beyond the study areas and laser scrambled effect on the top of the LiDAR, the point clouds are firstly cropped in the 3D digital model. Then an Octree Filter is applied to each scan. The purpose of the Octree Filter is to remove and merge the point cloud data to a better-organized format with relatively smaller size without losing any valid data. After the application of Octree filter, one point in the gravity center of surrounding points could represent a large number of points. The differences are shown in Table 2.

Position	Before Octree Filter	After Octree Filter
Scan 7	166,198,937 points	27,915,969 points
Scan 8	135,187,698 points	21,138,648 points

Table 2: Amount of data points before and after the application of Octree Filter. Examples of Scan 7 and Scan 8.

The last step is to apply the Terrain Filter to each scan (Figure 9). The objective of this filter is to separate the off-terrain points (e.g. vegetation, small objects, moving objects such as people, animals, etc.) from the major terrain points. After all scans are applied with these filters, the 3D digital model is shown by merging all scans together on the basis of common highly reflected objects from one scan to the next. The 3D digital

model can be performed in a single window with a specific view type for different purposes. Twenty percent overlap gives a good combination for this research.

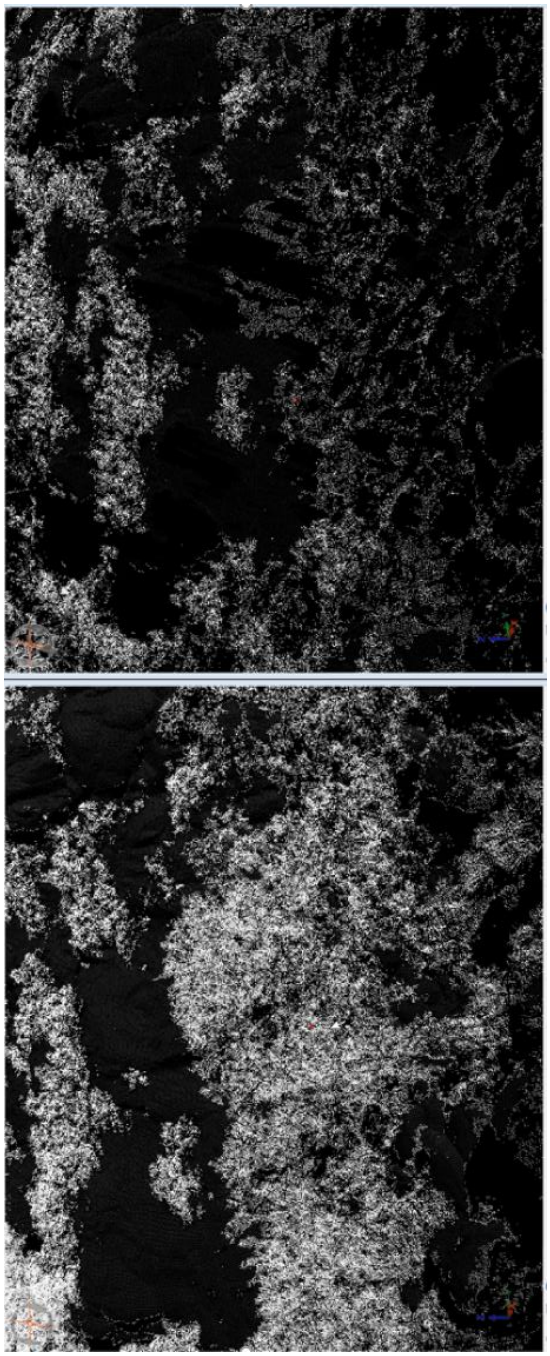

Figure 9: Comparison between raw point clouds and Terrain filter applied point clouds for the same location. Left picture shows raw point clouds with substantial vegetation on top of the outcrop. Right picture shows point clouds after Terrain Filter applied.

3.2.3 Post Processing

The resolution of this LiDAR DOM can reach to one-centimeter scale. Because of the post-depositional compaction, the bedding dips at the slope range between 2° - 65°. Therefore, the scanner coordinate system is preferred for the 3D digital model display in this study to easily trace the beds and interpret the sequence stratigraphic section. Owing to the differences in laser reflectance among carbonate rocks, sandstones, and vegetation, the reflectance view type outputs different colors. While the carbonate rocks provide relatively high reflectance values, sandstones and vegetation output relatively low reflectance values. The two-detailed measured sections (MCK 1 and MCK 2) are manually positioned in the 3D digital model from field work or that are georeferenced with GPS. The difference between the model and the outcrop is reduced by calibrating the geological interpretation from the fieldwork data into the model. The stratigraphic interpretation is digitalized by directly adding polylines in the Rescan software.

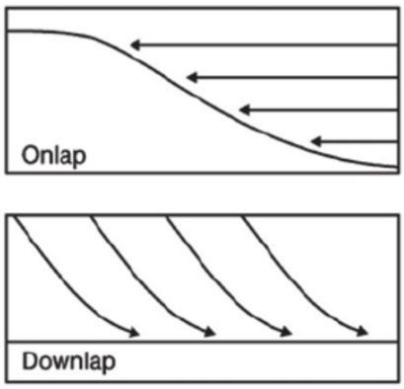

Figure 10: Schematic of strata terminations of onlap and downlap. When initially horizontal strata terminate progressively against an initial inclined surface or inclined strata terminate updip against a greater inclination, the base-discordant relation is defined as onlap. While when initially inclined strata terminate downdip against an initially horizontal or inclined surface, the base-discordant relation is defined as downlap. Modified by Mitchum (1991).

The bedding termination is useful to discriminate the location of the depositional setting of a system tract and/or from one sequence geometry to another (Mitchum, 1991). Within the 3D digital model, the bedding terminations are then interpreted by tracing the observed bedding planes. The bed terminations include onlap, downlap, offlap, and truncation. When initially horizontal strata terminate progressively against an initial inclined surface or inclined strata terminate updip against a greater inclination, the base-discordant relation is defined as onlap (Figure 10). While when initially inclined strata terminate downdip against an initially horizontal or inclined surface, the base-discordant relation is defined as downlap (Figure 10) (Mitchum, 1977). Toplap and truncations are not examined in this study because the study area is restricted to the slope. Details are discussed in Chapter 4.2.2.

3.3 X-Ray Fluorescence

The X-Ray Fluorescence (XRF) measurements are taken from a Thermo Fisher Scientific Niton XL3t Analyzer in this research. It is a hand-held device which allows the convenient operation by nontechnical personnel to use in the field for getting reliable and real-time elemental composition for each sample. The XRF analyzer shoots a primary X-ray source and then measures the fluorescence X-ray emitted from a sample (Thermo Fisher, 2010). It provides a standard analytical range of up to 41 elements while measured under TEST ALL GEO mode for 210 seconds, e.g., silicon (Si), iron (Fe), titanium (Ti), zirconium (Zr), aluminum (Al), potassium (K), phosphorous (P), calcium (Ca), strontium (Sr), magnesium (Mg), manganese (Mn), molybdenum (Mo), vanadium (V), cobalt (Co), nickel (Ni), copper (Cu), thorium (Th), and uranium (U). Most of the measurement are taken directly on the fresh and relatively flat surface at outcrops on an area of 3-4 cm^2.

For those outcrops without flat surface, the rock pieces are knocked down and shaped by rock hammer to take the XRF measurements. As this study area is along a National Park trail, if samples were required to be shaped, they were done so off the trail and extrapolated in position. To examine the reliability of measured XRF data, XRF measurements were taken before and after washing for a sample collected from the study area. The preliminary data show that for these carbonates, data obtained from the field before and after washing are not substantially different (Appendix I). The data are first restored in the analyzer and then are exported into Excel through Thermo Software on the laptop. The results of all data are recorded in parts per million (PPM).

3.3.1 Hierarchical Cluster Analysis

Cluster analysis is a fundamental data statistical technique employed in a variety of fields. When supplied with abundances of all elemental data (totally twenty-seven elements at each data point), the interpretation and understanding can be a problem. To study the rock as a whole, rather than individual elements, a technique is introduced as hierarchical cluster analysis. A hierarchical cluster analysis is conducted to examine the similarities among them and elements in the same cluster are more similar to each other than those in others. Software utilized for the hierarchical cluster analysis was Minitab.

3.3.2 Lithologic Composition

The XRF data can be used to study the lithologic composition at each data point. The software used in this research is an unpublished Microsoft Excel program written by Dr. John D. Pigott (personal communication). Following input of the concentrations of Fe, S, Mg, Ca, Al, Si, and Sr, the program is able to display the percentage of different minerals of feldspar, mica-clay, quartz, gypsum, calcite, dolomite, and pyrite in a sector diagram for a single measured spot (Figure 11). After linking all the elemental data with their depths data, a lithology log was made to display the composition variations changing along the depth of measured sections.

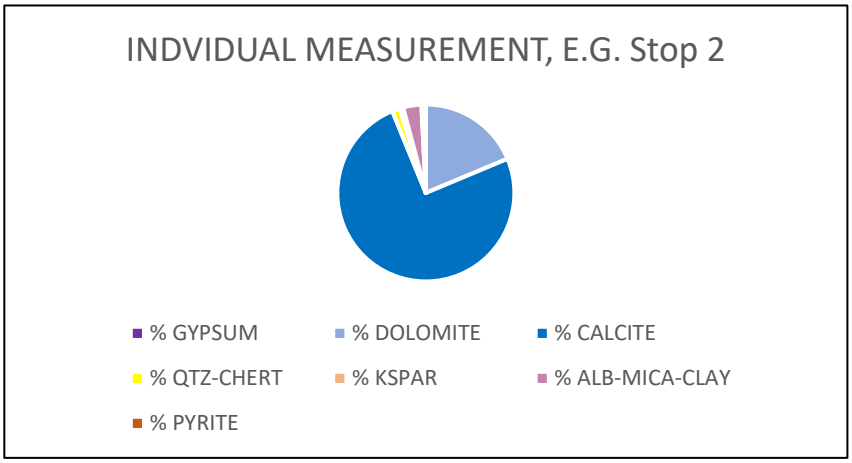

Figure 11: An example of the sector diagram showing lithologic composition at stop 2.

3.3.3 XRF Pseudo Gamma Ray

The gamma ray log is an efficient tool to study the sequence stratigraphy because of its general relationship with interpreting paleoenvironmental stacking patterns (Thermo Fisher Scientific, 2010). For spectral gamma ray(SGR), the equivalent value can be calculated from abundances of Thorium (Th) in ppm, Uranium (U) in ppm and Potassium (K) in weight percent (Doveton and Merriam, 2004). The equation is:

$$SGR = 4 \times TH + 8 \times U + 16 \times K$$

Where abundances of Th, U, and K can be collected from XRF analyzer used in the field. Once these elemental abundances are measured at each XRF measurement position, a pseudo spectral gamma ray log then can be created.

3.3.4 Molybdenum-Uranium Proxies

Tribovillard (2012) has revealed the quantitative relationships between marine paleoredox conditions and enrichments of Mo, U, and Mo: U ratios after studying intensive present marine systems. This method allows researchers to analyze even the information about organic matter is not available or even impossible to determine.

The first step is to determine whether elements are relatively enriched or depleted. This is done using the method introduced by Wedepohl (1991) and McLennan (2001). In many studies, Aluminum has been shown to be a good proxy with very little ability to move during diagenesis in most sedimentary deposits (Brumsack, 1989; Calvert and Pedersen, 1993; Morford and Emerson, 1999; Piper and Perkins, 2004). Here, the enrichment factors (EF) are calculated by this equation:

$$EF_{element\ X} = (X_{sample} / Al_{sample}) / (X_{average\ shale} / Al_{average\ shale})$$

Where X and Al represent the weight percent concentrations of elements of X and Al. The normalization is using post-Archean average shale compositions of Taylor and Mclennan's (1985).

Elements	Main species in oxic seawater and oxidation state	Average concentration in seawater (nmol/kg)	Residence time in seawater (kyr)	Speciation in reducing conditions	Average upper crust abundance (μg/g)[a]	Post-Archean average Australian shale (μg/g)[b]	Average shale (μg/g)[c]
Mn	MnO_2 and Mn^{2+}/Mn(IV) and Mn(II)	0.36	0.06	See text	600	1400	850
Ba	Ba^{2+}	109	10	See text	550	650	650
Cd	$CdCl^{+}$/Cd(II)	0.62	50	CdS/Cd(II)	0.1	0.1	0.3
Co	Co^{2+}/Co(II)	0.02	0.34	CoS/Co(II)	17	20	19
Cr	Dominantly CrO_4^{2-}/Co (VI)+$Cr(OH)_2^{+}$ and Cr $(OH)_3^0$/Cr(III)	4.04	8	$Cr(OH)_2^{+}$, $Cr(OH)_3$, $(Cr,Fe)(OH)_3$/Cr(III)	83	100	90
Cu	$CuCl^{+}$/Cu(II)	2.36	5	CuS CuS_2/Cu(I)	25	75	45
Mo	MoO_4^{2-}/Mo(VI)	105	800	Thiomolybdates	1.5	1	1.3
Ni	$NiCl^{+}$, $NiCO_3$, Ni^{2+}/Ni(II)	8.18	6	NiS/Ni(II)	44	60	68
U	$UO_2(CO_3)_3^{4-}$/U(VI)	13.4	400	UO_2, U_3O_7 or U_3O_8	2.8	0.91	3
V	HVO_4^{2-} and $H_2VO_4^{-}$/V(V)	39.3	50	VO^{2-}, $VO(OH)_3^{-}$, $VO(OH)_2$/V(IV) V_2O_3, $V(OH)_3$/V(III)	107	140	130
Zn	$Zn^{2+}ZnCl^{+}$/Zn(II)	5.35	50	ZnS, (Zn,Fe)S	71	80	95
Al					80,400	84,000	88,900

Table 3: Geochemical data of post-Archean average shale compositions (Taylor and Mclennan, 1985). The values of X average shale and Al average shale can be read through the table.

Minor enrichments in U and Mo are characteristics of oxic conditions. Modest enrichment (EF < 10) in U and Mo are characteristic of suboxic conditions, and U-EFs are often greater than Mo-EFs. In anoxic to euxinic conditions, the strongest enrichment (EF > 10) in U and Mo exists with higher Mo to U ratio. Mo: U ratios can also be used as a tool to interpret the redox conditions. Low Mo: U ratios (below 0.3×SW) are found in suboxic environments. Moderate Mo: U ratios (~1×SW) are found in anoxic environments and high sediment Mo: U ratios are found in strongly euxinic environments (Tribovillard, 2012).

Chapter 4: Observation and Interpretation

4.1 Trace Element Proxies

4.1.1 Gamma Ray Logs and Pseudo-Gamma Ray Logs

Gamma rays are defined as the electromagnetic radiation from an atomic nucleus during the decay of an unstable element. Unlike including contributions from all radiative elements for total gamma ray measurements, the spectral gamma ray only counts the energy of the radioactive elements of potassium, uranium, and thorium decay. Therefore, minerals that fix K, U, and Th, such as clay minerals and K-feldspars, are the dominant sources of spectral gamma radiations (Hampson et al., 2005).

To examine the reliability and accuracy between the XRF derived pseudo GR and the spectral GR, eight cross-plot graphs are made to check the difference. The spectral gamma ray data were collected by Zhou (2014) at the positions close to the measurement positions in this study. The cross-plots comparison between SGR values and XRF derived SGR (PGR) values in toe-of-slope sections and foreslope sections are shown in Figure 12.

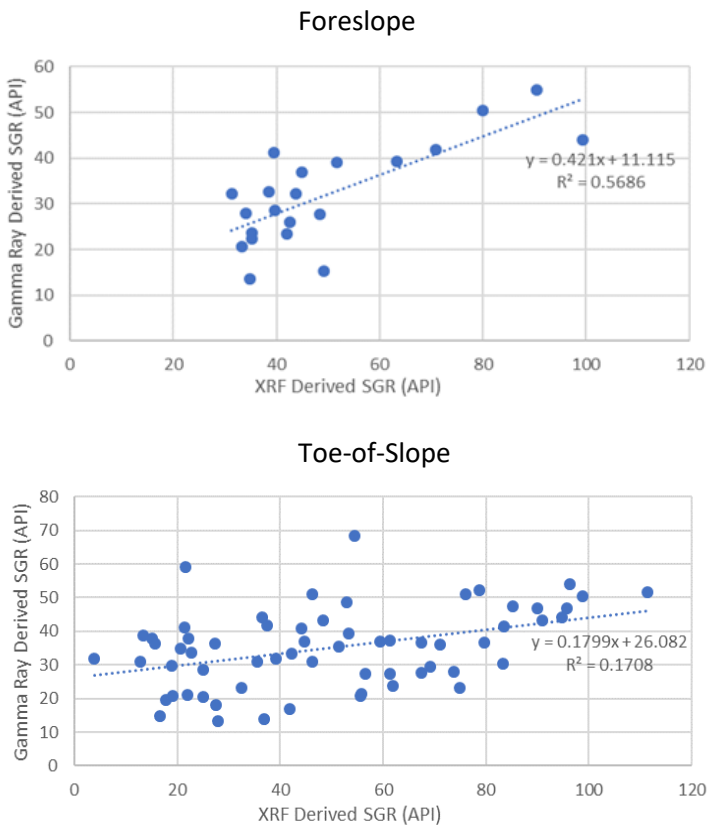

Figure 12: Cross-plots of comparison between SGR values and XRF derived SGR (PGR) values in toe-of-slope sections and foreslope sections.

Figure 12 illustrates that both for the toe-of-slope and foreslope the relationship between the pseudo gamma ray and spectral gamma ray values is significant at the P = 0.01 levels (Rohlf and Robert, 1969). (For toe-of-slope, N = 69 - 2, the correlation coefficient is 0.412 which is statistically significant at the P = 0.01 level; for the foreslope, N = 21 - 2, the correlation coefficient is 0.748 which is statistically significant at the P = 0.01 level.)

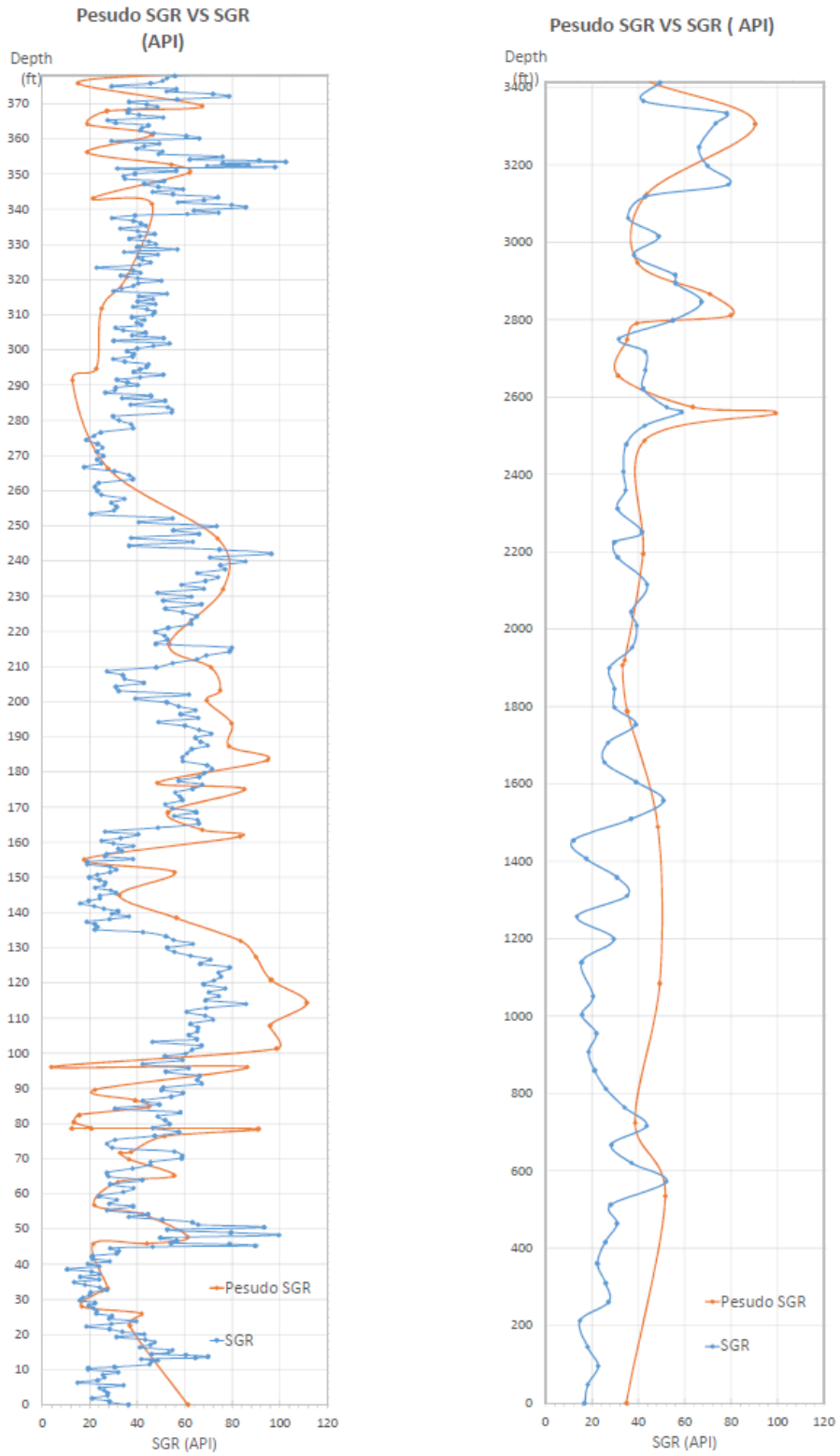

Figure 13: Comparison between spectral gamma ray curves and pseudo gamma ray curves in foreslope and toe-of-slope slope sections. The spectral gamma ray curves are highlighted in blue lines and the pseudo spectral gamma ray curves derived from XRF data are highlighted in orange lines.

The comparisons between the pseudo gamma ray logs and the spectral gamma ray logs of two measured sections are shown in Figure 13. The relatively strong correlations between these curves demonstrate the utility of pseudo spectral gamma ray log construction from XRF data. Differences may be attributed to the overlap of spectra from the other XRF element.

With the method discussed in the Chapter 3.3.2, the lithology logs are created to help reveal and confirm the correlations between pseudo gamma ray values and lithology. In general, the pseudo gamma curves are observed to show good covariations with radioactive minerals such as K-feldspar and mica (Figure 4.14 and Figure 4.15). High gamma ray values are more observed within siliciclastic units and low gamma ray values are more commonly observed within carbonate units in the study area. These gamma ray characteristics were also observed in the similar mixed siliciclastic-carbonate environment (e.g., Krassay, 1998). The exceptions are noticed at the lower parts (0 ft – 46 ft) and the upper parts (316 ft – 378 ft) in toe-of-slope sections and at the upper parts (2800 ft -3400 ft) in foreslope sections. The fluctuation of the pseudo gamma ray in those parts are not associated with lithologies but may be contributed by carbonate muds that possess relatively high gamma ray count during long-term deposition under unchanged environments.

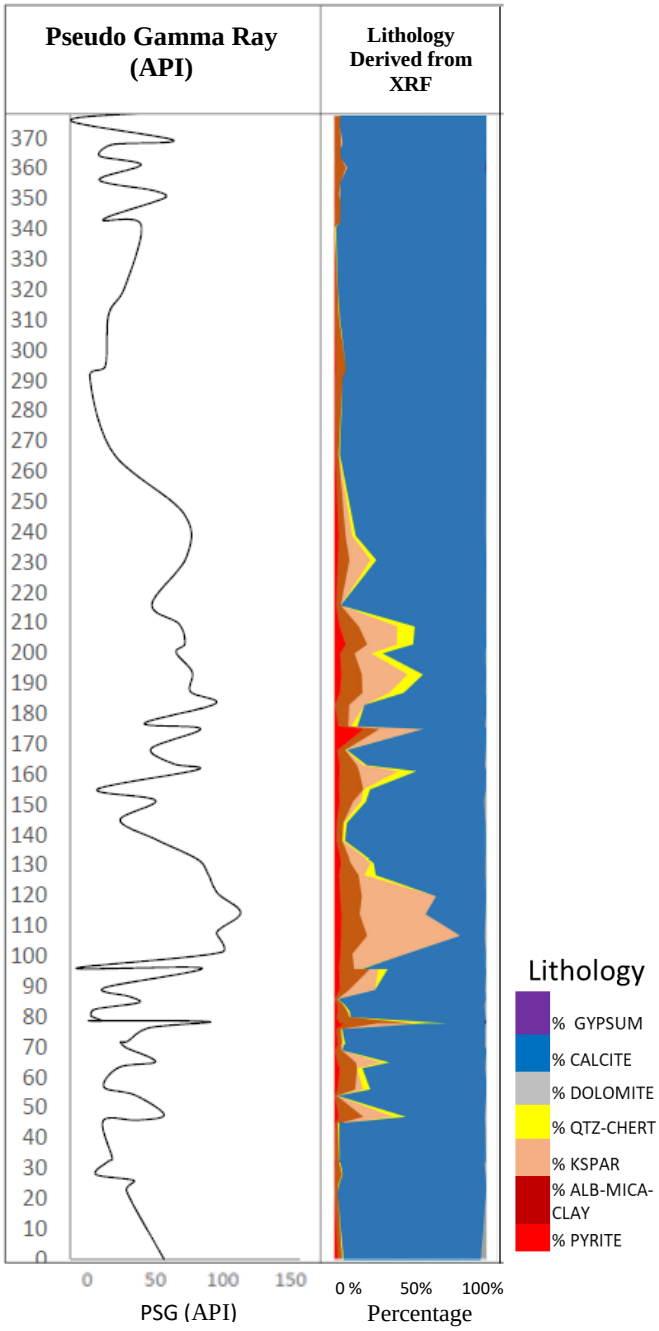

Figure 14: Correlation between pseudo gamma ray logs and lithology logs in toe-of-slope sections.

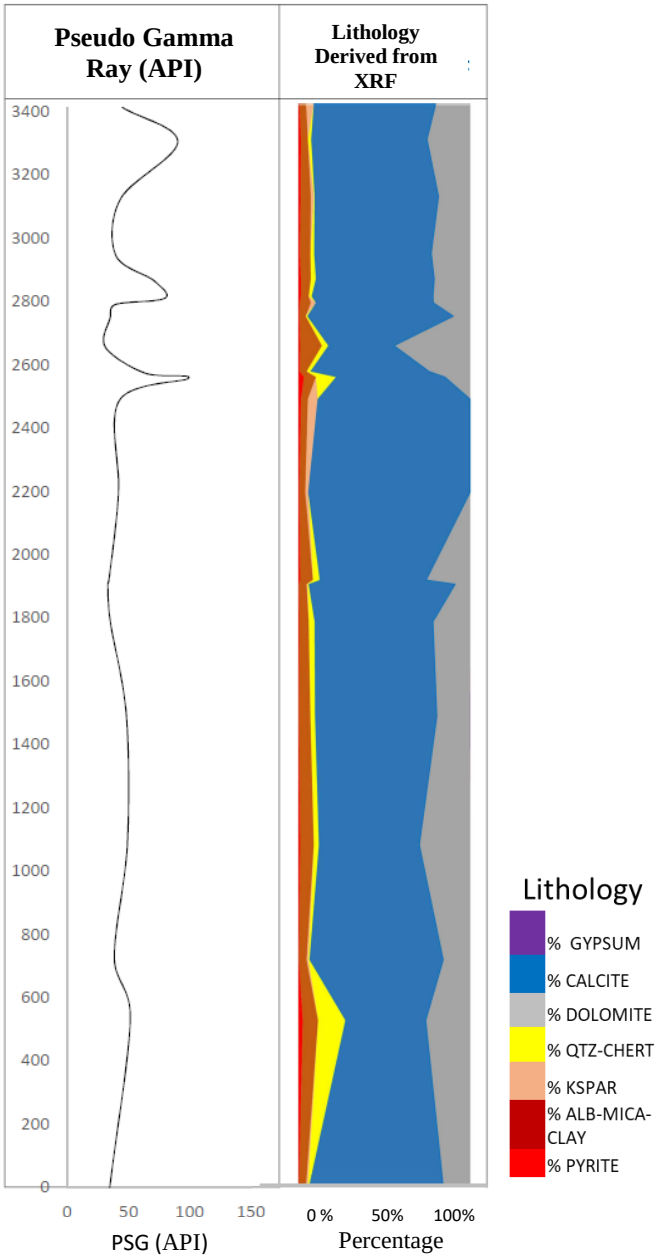

Figure 15: Correlation between pseudo gamma ray logs and lithology logs in foreslope sections.

4.1.2 Hierarchical Cluster Analysis

Major elements, minor elements, and trace elements are all included to characterize and correlate strata. In general, stratigraphic units are often characterized by distinct elemental signatures according to different depositional environments such as

paleodepositional environments and paleooxygen conditions (Riquier et al., 2005). Therefore, elemental proxies have been proved to be a good quantitative tool for those units that cannot be studied under microscopes.

Among all 41 elements detected from the hand-held XRF analyzer, some of them show the similar trends after plotting them in depth, but some of them do not. With the knowledge of characteristics of each element, a hierarchical cluster analysis that comprisies 27 reliable elements was made through the statistical software of Minitab. The aim is to testify the similarities and to determine which elements could serve as good proxies in the study area.

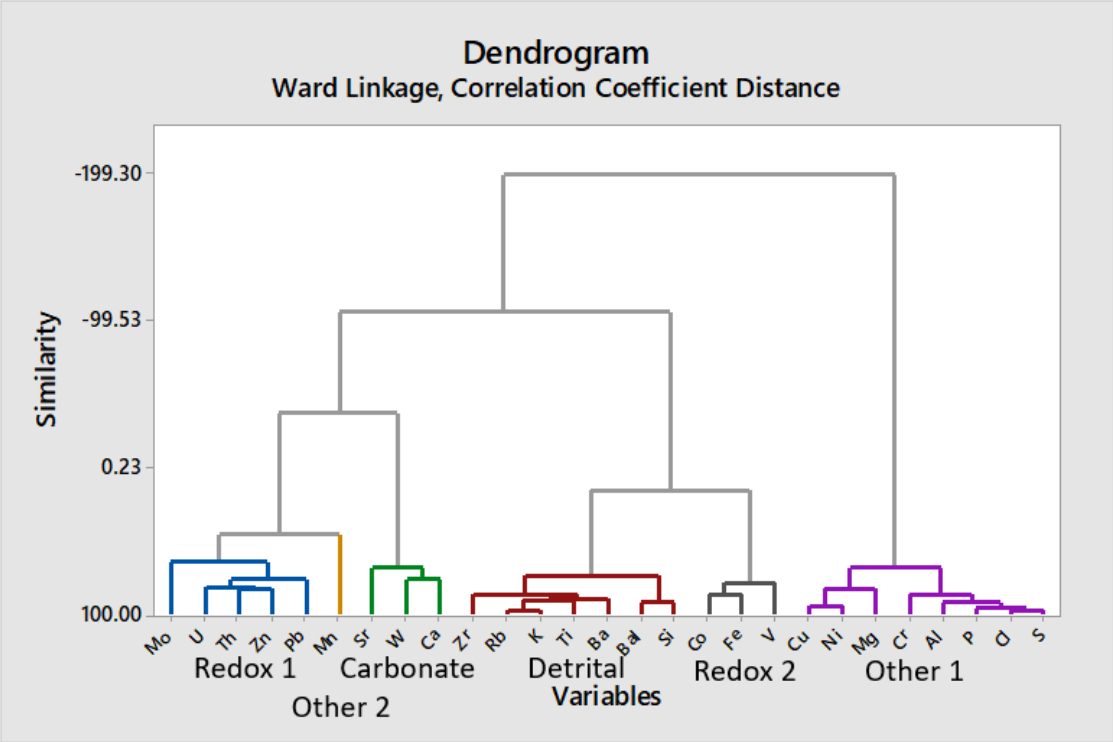

Figure 16: The result of hierarchical cluster analysis. Six major clusters are identified and highlighted in colors.

Clusters	Variables
Redox 1	Mo U Th Pb Zn
Detrital	Zr Ti K Si Rb Ba Bal
Carbonate	Sr Ca W
Other 1	Cu Ni Cr Al P Cl S Mg
Redox 2	V Co F
Other 2	Mn

Table 4: Six major clusters and their associated elements.

The elemental order on the hierarchical cluster analysis map was based on similarities between each element. There is a total of six major clusters identified in Figure 16 and Table 4. The clusters with their related elements are listed in Table 5 and are given names referring to the elemental implications. Because not all elements could be served as qualified proxies.

Groups	Elemental proxies
Siliciclastic Proxies	Si, Ti, Zr, Si/Ti, Al, K
Carbonate Proxies	Ca, Sr
Redox Proxies	U, Mo, U & Mo, V, Ni, Cu

Table 5: Selected elemental proxies in siliciclastic proxies, carbonate proxies, and redox proxies.

Elemental proxies within the same clusters are selected to form three proxy groups associated with provenance and paleoredox conditions. The three proxy groups are named siliciclastic proxies (Si, Ti, Zr, Si/Ti, Al, K), carbonate proxies (Ca, Sr), and redox proxies (U, Mo, Mo & U, V, Ni, Cu) (Table 5). Here, “siliciclastic” is used as the general term for the sandstone and siltstone deposited along the slope to basin

4.1.3 Siliciclastic-Carbonate Proxies

To better interpret the relationships between stratigraphic units and link them to paleoenvironments, it is necessary to first understand reactions of different elemental proxies to environmental changes, to be enriched or to be removed.

Terrigenous-originating elements show comparable distribution patterns in logical opposition to carbonate content. Zr, Ti, Si, K and Al occur mainly in terrigenous silicates and oxides, so form the detrital load, typically land-derived through erosion of continental rocks and therefore indicative of sediment transport from land to the deep-sea. The variations between siliciclastic proxies and carbonate proxies are able to illustrate the provenance information. The enrichment of Ti and Zr is the indicator of the abundance of continental sediments. Ti has also been widely used as a terrigenous indicator (e.g. Yarincik et al., 2000; Pigott, 2004; Treanton, 2014; Turner, 2016). Ti and Si are usually used as proxies for terrigenous sediment delivery in provenance studies. As it is often found in detrital quartz, biogenic quartz, feldspars, and clays. The Si/Al ratio can provide a rough approximation of the biogenic quartz amount (Wilde et al., 2004). K is usually related to the terrestrial siliciclastics and is often used as an important terrigenous proxy. Variations in K and Ti relate to higher terrestrial discharge into the basin, either through higher precipitation and runoff or through more coastal erosion by storms or currents. Lower K and Ti are attributed to a relative decrease in terrestrial discharge together with pelagic deposition or interpreted as a function of eolian dust inputs (Tribovillard, 2006). To be noted, Ti is regarded to be a better proxy associated with deposits of detrital provenance according to the result that Ti appears to show better similarities with other siliciclastic proxies in the study area. Therefore, Si/Ti ratio is used

in this study to distinguish the biogenic silica or detrital silica instead of Si/Al ratio. Therefore, with the result of the hierarchical cluster analysis, the elements in the group of siliciclastic proxies are referred to be Ti, Zr, Si, Si/Ti, Al, K.

In toe-of-slope sections, all values of siliciclastic proxies observed remain constantly low between 0 ft to 45 ft, which indicates the terrestrial sediments deposited during this stage are minimal. Downward from 45 ft, proxies exhibit elevated concentrations and fluctuate within nearly the same trends until 88 ft. The values of Si, Ti, Zr, and K increase greatly from 88 ft and soon decrease to the moderate level at 93 m. Then those values are marked with a boost at 100 m and slightly decrease but are still maintained relatively high until 134 ft. Si, Ti, Zr, Al, and K reach a low but Si/Ti ratio increases from 134 ft to 157 ft. This implies the biogenic Si deposited during relative high sea level is not diluted by detrital grains. Two peaks occur from 157 ft to 163 ft and from 170 ft to 177 ft and a relatively high value range occurs from 196 ft to 213 ft for Si, Ti, Zr, and K, which indicates large volumns of detrital sediments. Si, Zr, and Al exhibit a low whereas Ti stays at moderate values between 213 ft and 220 ft, which suggests moderate detrital sediment input. Another peak between 232 ft to 240 ft is also observed for Si, Ti, Zr and K. In the Lamar Limestone unit from 250 ft to 376 ft, all proxies remain low (Figure 4.17).

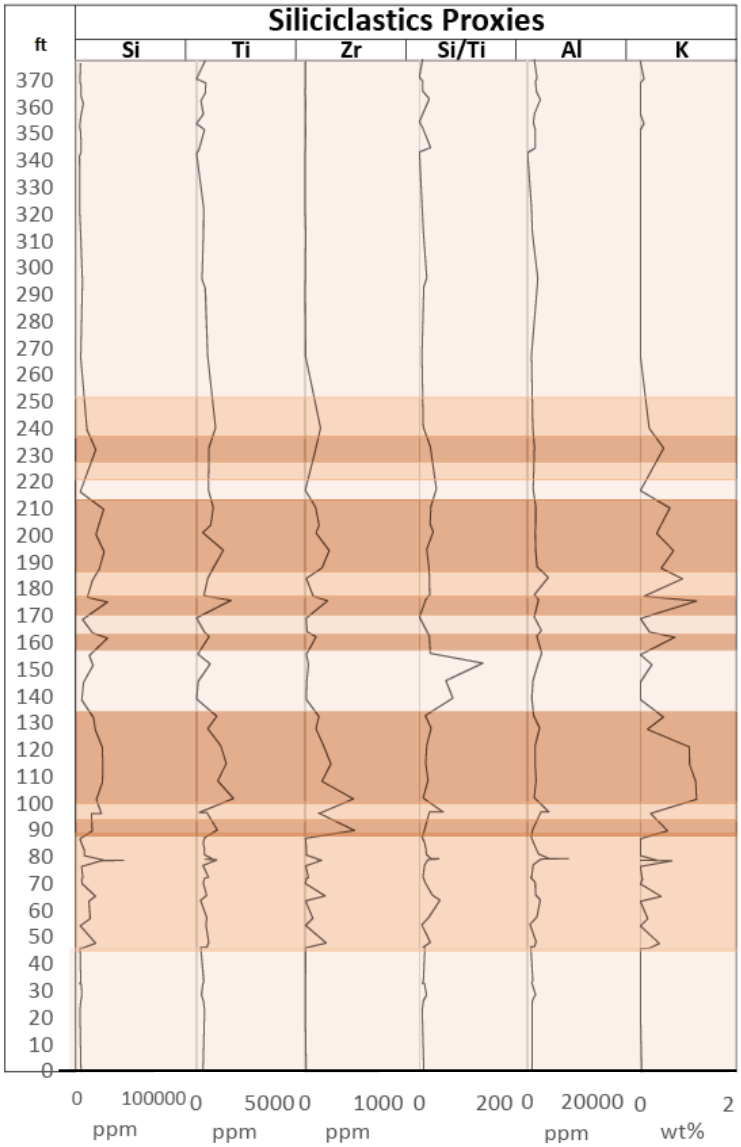

Figure 17: Variation of siliciclastic proxies in toe-of-slope sections. The darker colors represent higher values.

In the toe-of-slope section, all the siliciclastic proxy ratios perform a good covariation along this section except the Si/Ti ratio. This ratio represents the percentage of biogenic silica to overall silica and performs a roughly negative relationship with other proxies. Though the proxies as shown have different magnitudes, their overall trends and strong correlations are observed in matching peaks and troughs (Figure 17; Figure 18).

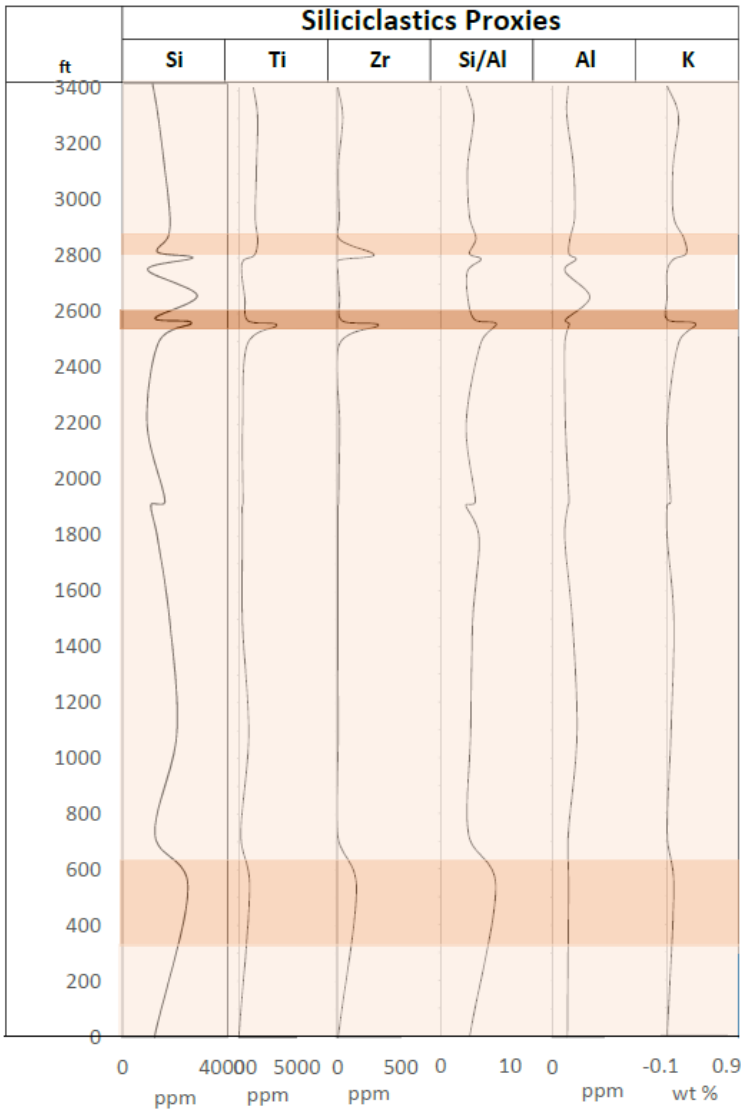

Figure 18: Variation of siliciclastic proxies in foreslope sections. The darker colors represent higher values.

The concentrations of Ca, Sr and Mg are major carbonate-related elements. Ca is often used as an effective carbonate indicator for stratigraphic frameworks (Bahr et al. 2008). Low values of Ca may be associated with the dissolution of carbonate or dilution effect by increasing terrigenous materials and lack of carbonate mineral deposition (Revel et al., 2010). Since Ca is also supplied from terrigenous sources, the co-variation of both Ca and Sr indicates the provenance of biogenic carbonate. Sr can also be used to identify the carbonate rocks type (Richter et al. 2006). Mg is an important element to represent

the presence of dolomite which is extensive on the shelf, with its lack of hierarchical association with Ca and Sr (Figure 16). In this study, Ca and Sr are selected to be the carbonate proxies.

In Figure 19, the values of Sr are observed to remain relatively low with minor fluctuations between 0 ft to 298 ft and between 364 ft to 376 ft. The distinct Sr peak is observed between 298 ft to 364 ft and is consistent with values of Ca remaining at a relatively high level. Ca fluctuates greatly with several large variation ranges. The high values of Si and Ca are indicative of high volumes of deposited carbonates. Even though the high values of Si and Ca can also be observed in the sand unit, it could be the result of eroded skeletal carbonates from slope failures occurring in the reef zone at the slope top.

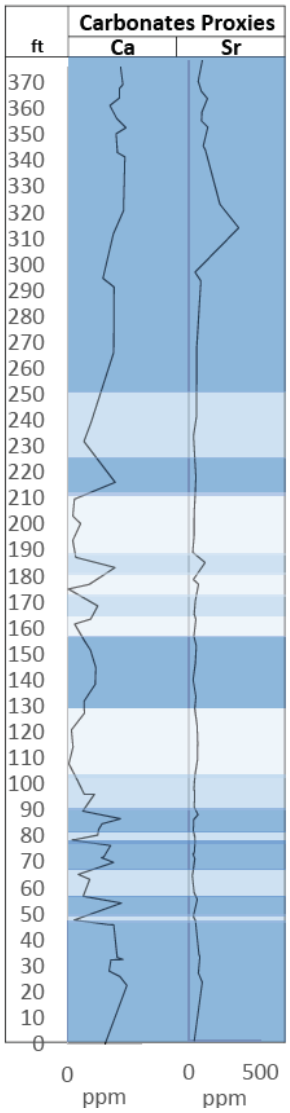

Figure 19: Variation of carbonate proxies in toe-of-slope sections. The darker colors represent higher values.

In foreslope sections, the proxies show less variations and are more homogeneous than those of toe-of-slope sections (Figure 20). A possible explanation for this phenomenon is that this section locates at the geographical high position with mostly carbonate deposits but little siliciclastic deposits. Detrital sediments are not able to be deposited at such high dip angles common to carbonates and have a greater flux energy. Instead, they bypass foreslopes and are deposited at toe-of-slope sections. The stratigraphic units deposited under nearly the same environment attribute to the small

variation ranges here. Similarly, the provenance interpretation is consistent with the contents discussed in toe-of-slope sections.

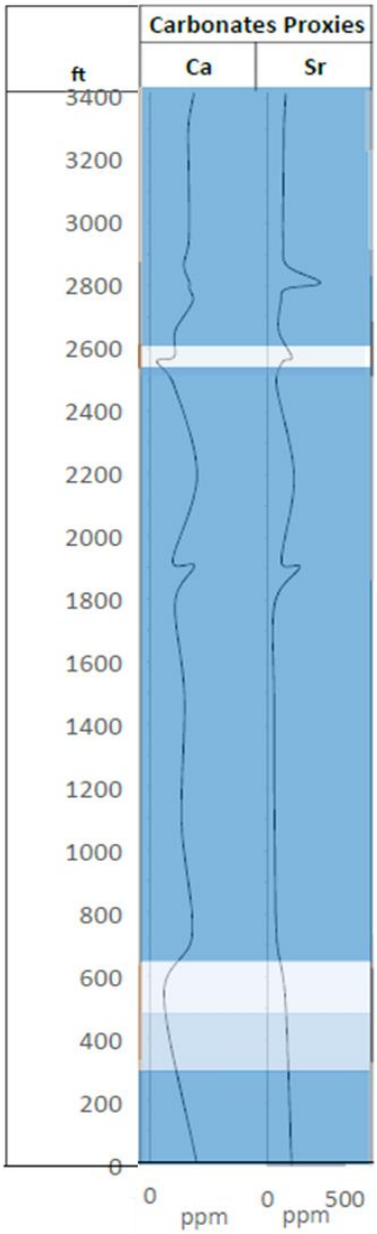

Figure 20: Variation of carbonate proxies in foreslope sections. The darker colors represent higher values.

4.1.4 Redox Proxies

Owing to the complexity of elemental origins and removal, it is a better method to analyze the environmental conditions by using a suite of proxies rather than any single

proxy. Mo alone cannot be used as a redox proxy. Algeo and Rowe (2012) suggest the single use of Mo concentrations is still questionable owing to the 'basin reservoir effect' of different paleogeographies and thus need to be coupled with other paleoredox proxies. Therefore, Mo and U together are considered to be reliable redox indicators with minimal detrital affection and are thus selected as representative proxies for paleoredox-condition reconstruction (Rimmer, 2004; Algeo, 2007). Cr has limitations for its use as a paleoenvironmental proxy owing to its complex transportation and enrichment processes. The Co concentration is strongly associated with the increasing clastic input. Because the enrichment of Ni and Cu is not found to be greatly increased in rapidly reducing environment, the abundance of Ni and Cu can be only used as an indicator of relatively high organic matter flux (Tribovillard et al., 2006). To be noted, if Ni and Cu have good correlations with Al, it indicates that the enrichments are mostly contributed by the detrital sediments and the proxies are not reliable to reveal the variation of organic matter (Tribovillard et al., 2006). Mn alone cannot be used as a redox proxy because of its high mobility in reducing sediments. Therefore, with the result of the hierarchical cluster

analysis, the elements in the group of redox proxies are referred to be Mo(EF), U(EF), Mo & U, V, Ni, and Cu.

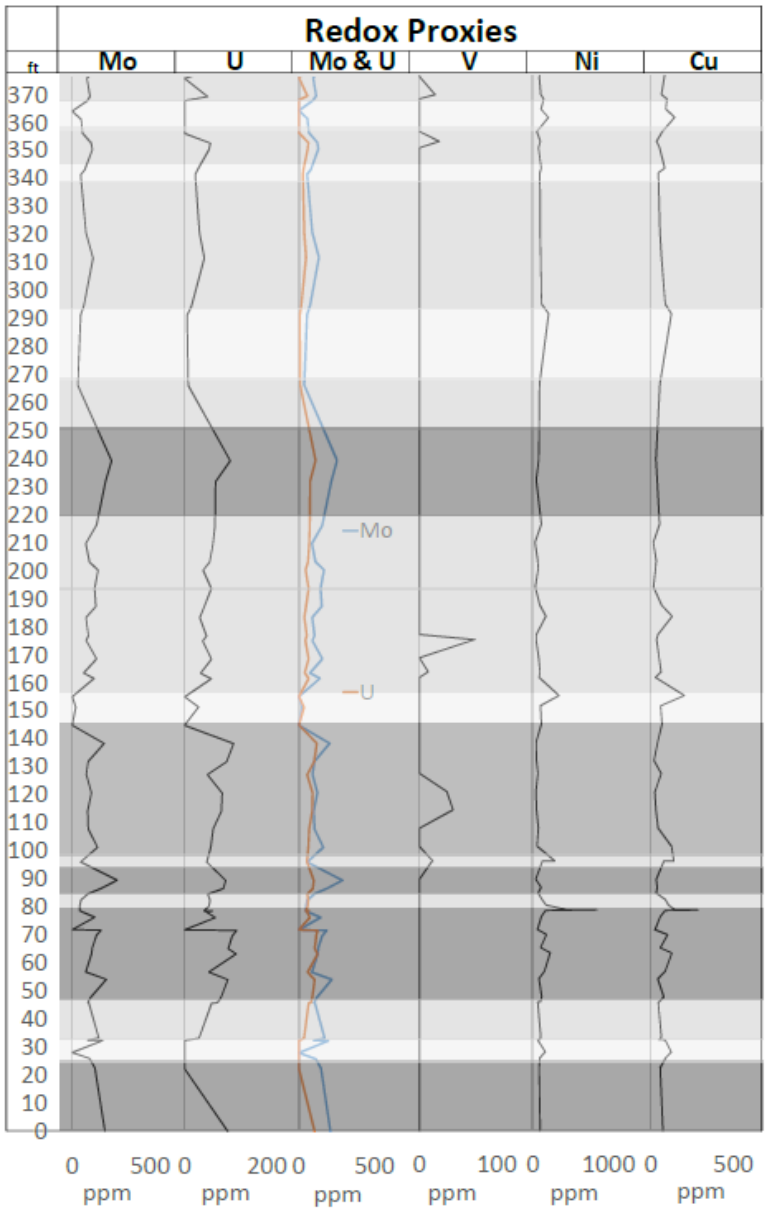

Figure 21: Variation of redox proxies in toe-of-slope sections. The darker colors represent higher values.

Along the whole measured sections in the slope, good covariations are observed both between Mo and U and between Ni and Cu. Mo and U exhibit a larger range of variations compared to Ni and Cu. V shows several distinct peaks and corresponding to the relatively high Mo and U values. The darkest zone in Figure 21 and Figure 22

represent the sections coupled with more reducing environments. Within these sections, the values of Mo, U, Ni, and Cu are relatively high. The rest of the sections are characterized by relatively moderate to low values of the redox proxies.

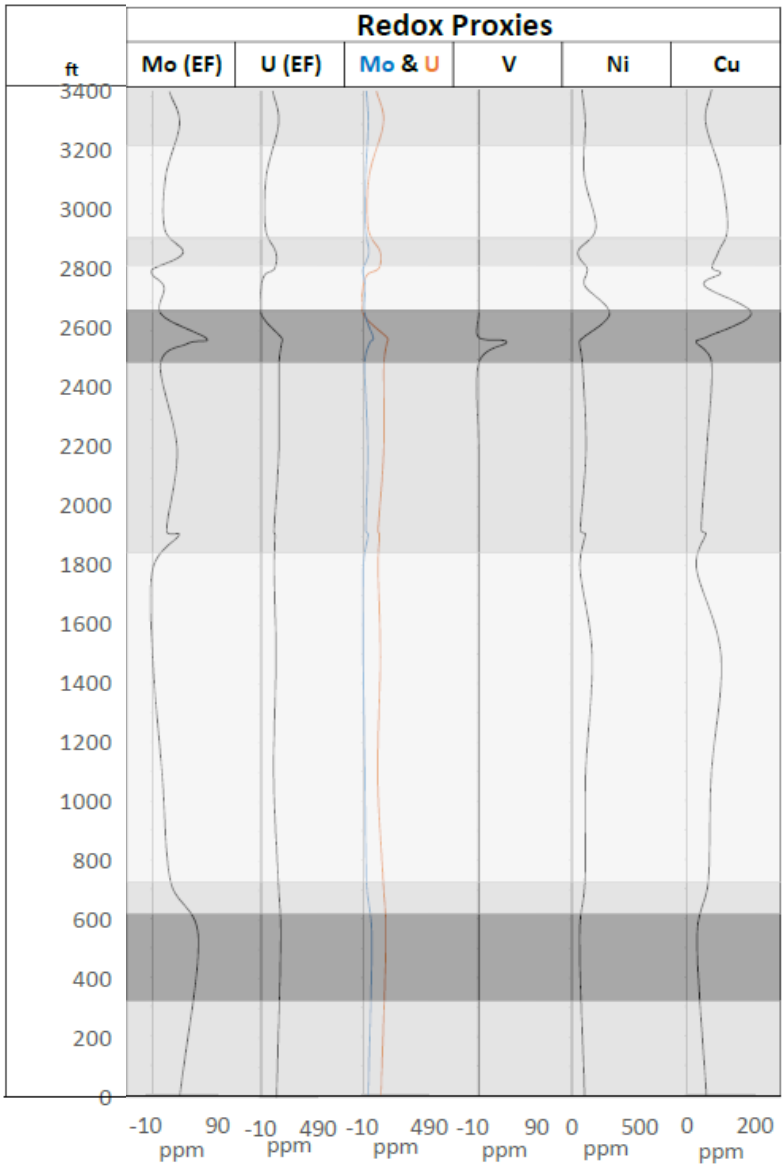

Figure 22: Variation of redox proxies in foreslope sections. The darker colors represent higher values.

4.1.5 Paleoredox

The study of paleoredox conditions is to understand whether pre-existing organic-matter was preserved or decomposed during deposition (Sagemanet al., 2003; Mort et al., 2007). The variations of XRF elemental concentration provides important information for reconstruction of paleoredox conditions. In more oxidizing conditions, elements of redox proxies tend to be more soluble and less commonly found in the bottom-deposited strata. In more reducing conditions, elements of redox proxies tend to be less soluble and to be more preserved in bottom-deposited strata (Tribovillard, 2006).

In this study, the redox gradation (oxic, suboxic, anoxic and euxinic) are adapted to describing the conditions from oxidizing to reducing (Table 6). With the increasing consumption by aerobic organisms in oxic conditions, the dissolved oxygen becomes depleted in the water. This depletion results in the formation of suboxic conditions where oxygen concentrations are extremely low, but nonzero. As oxygen consumption continues and all free oxidants are exhausted, the redox turns into anoxic conditions and then euxinic conditions where hydrogen sulfide develops within the water columns. (Tyson and Pearson, 1991).

Redox classes	Oxic	Suboxic	Anoxic	Euxinic
H2S conditions	No free H_2S in the water column	No free H_2S in the water column	No free H_2S in the water column	Free H_2S present in the water column
O_2 concentration in bottom waters (ml O^2/l H_2O)	$[O_2] > 2$	$2 > [O_2] > 0.2$	$[O_2] < 0.2$	$[O_2] = 0$

Table 6: Redox classification of the depositional environments, by Tyson and Pearson (1991)

Redox proxies here refer to the redox-sensitive elements selected after the hierarchical cluster analysis. The detailed elemental changes along depth are discussed in Chapter 4.1.4. According to the widely accepted method introduced by Tribovillard et al. (2012), the paleoredox conditions are predicted through the comparation of enrichment factors of Mo, U, and Mo: U ratios to those factors in present-day seawater.

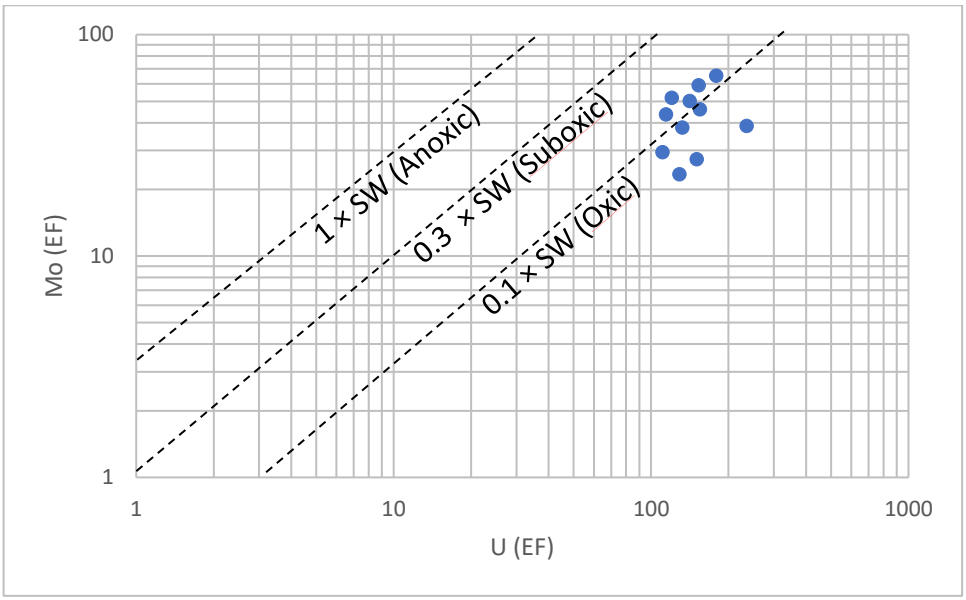

Figure 23: U (EF) vs Mo (EF) for samples from foreslope sections. It indicates the oxic to suboxic environment.

Figure 23 shows the Mo(EF) and U(EF) results of foreslope section analysis. Both Mo-EFs and U-EFs are greater than 10, with U-EFs greater than Mo-EFs. Mo: U ratios are located between 0.1-0.3 times of Mo: U ratios in present-day seawater, and most of the values are around 0.1 times Mo_{sw}: U_{sw} ratios. The results indicate oxic to suboxic environments.

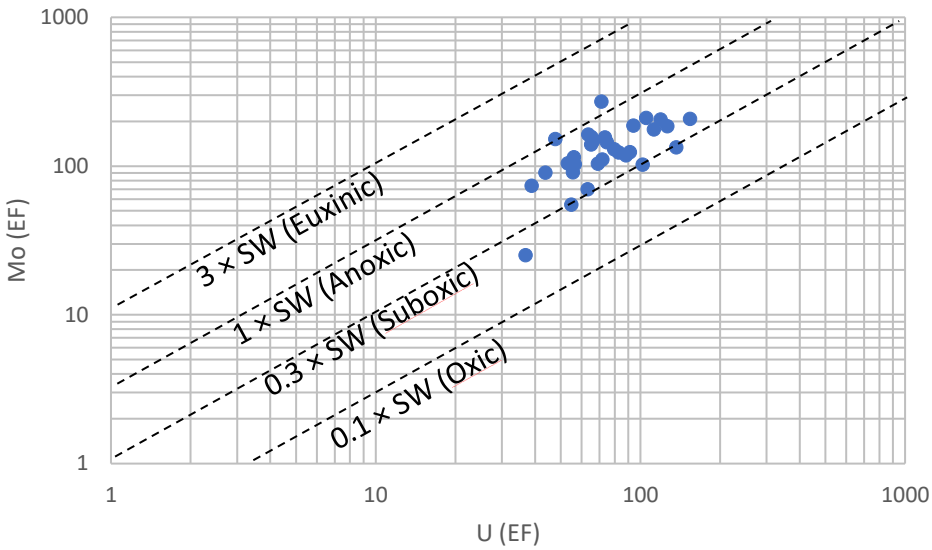

Figure 24: U (EF) vs Mo (EF) for samples from toe-of-slope sections. It indicates the suboxic to anoxic environments.

Figure 24 shows the Mo(EF) and U(EF) results of toe-of-slope section analysis. Both Mo-EFs and U-EFs are greater than 10. Mo: U ratios are mostly located between 0.3-1 times of Mo: U ratios in present-day seawater. The results indicate the suboxic to anoxic environments.

The variations of redox conditions are observed not only between foreslope and toe-of-slope sections, but also within each section. The results above reflect the shift from oxic/ suboxic and to suboxic/ anoxic conditions when the sediments are deposited deeper

along the slope. In addition, the results above reflect the variation existed even in the same depositional locations.

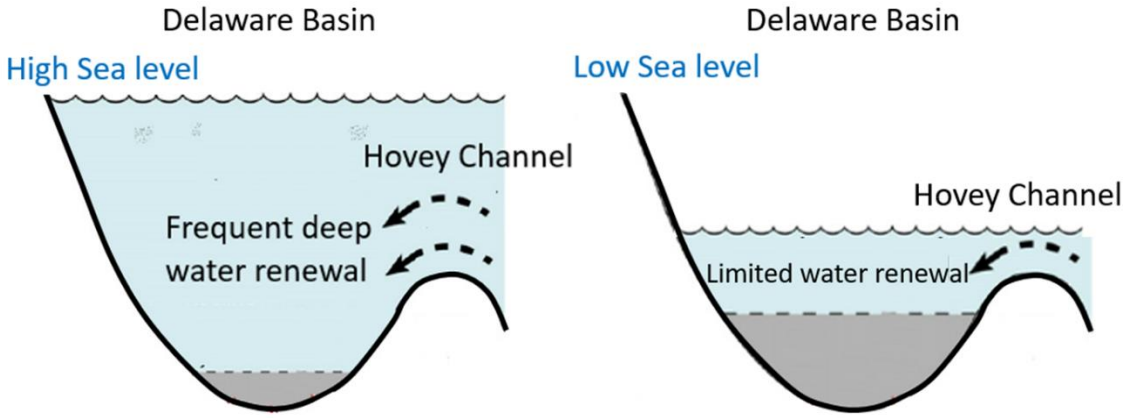

Figure 25: Schematic water circulation in Delaware Basin.

In suboxic or anoxic environments, the bioturbation, the process of displacing and mixing of sediment particles by faunal or infaunal organisms, is found to be significantly reduced (Sturdivant, 2012). The low concentrations of dissolved oxygen in suboxic and anoxic environments are likely triggered by degradation of increasing terrestrial organic matter input or restricted water mass renewal (Nance, 2015). The accompanying enrichment of organic matter can be shown on the variations of Ni and Cu. From the columns of elemental variation along depth (Figure 21; Figure 22), the values of Ni and Cu remain almost constant at a low level. Therefore, the only way to attribute fluctuations in redox conditions is to suggest water mass circulations within the basin. During low sea level periods, the influx of marine-derived water from the Panthalassa Ocean was less. The water mass circulation was diminished and only occurred at the top from input of the Panthalassa Ocean through the relative narrow and shallow Hovey Channel (Figure 4). Therefore, the slope sections developed under suboxic to anoxic environments. During the high sea level periods, the Hovey Channel became larger and deeper. The well-

circulated water brought more dissolved oxygen from water of Panthalassa Ocean and the slope sections developed under oxic to suboxic environments as a result (Figure 25).

4.2 Sequence Stratigraphy

4.2.1 Reviews and Terminology

As a subdiscipline of stratigraphy, sequence stratigraphy is referred to the analysis of genetically related strata bounded by unconformities' and their correlative conformities within a time-stratigraphic framework. (van Wagoner,1995). It is useful to reconstruct the basin-fill history from the impact of relative sea-level change and for stratigraphic prediction. From the previous studies, there are various sequence stratigraphic models and each model may work best under particular circumstances (Catuneanu, 2002). Modern high-resolution sequence stratigraphy within carbonate systems has been studied by (van Buchem et al., 2002), Tucker (2002), Kerans (2002,2010), etc.

In the past thirty years, the sequence stratigraphy of the late Guadalupian strata in Guadalupian Mountains has been intensively studied. As a first order premise, the global climatic transition from Carboniferous icehouse to Mesozoic greenhouse made the higher order eustatic fluctuations well expressed in the stratigraphic record (Read,1998). Several studies have investigated the high frequency cycles in Seven Rivers, Yates, and Tansill formations in different canyons of the Guadalupian Mountains (Borer and Harris, 1991a; 1991b; Kerans and Harris, 1993; Borer and Harris, 1995; Osleger, 1998; Tinker, 1998; Osleger and Tinker, 1999; Kerans, 2000). Among these, most of the framework of late Guadalupian strata was set up based upon the study of the well-exposed shelf margin in McKittrick Canyon. The primarily accepted sequence-stratigraphic framework for Yates

and Seven River formation was established by Tinker (1998). Kerans and Kempter (2002) later integrated Tinker's work and conducted the hierarchical stratigraphic analysis for the whole Guadalupe Mountains. In those studies, the stratigraphic framework was adapted after the sequences hierarchical framework made by Van Wagoner (1991) and the Upper Yates-Tansill formation were interpreted into a 3rd-order composite sequence (CS) containing four 4th-order high-frequency sequences (Y5/6/T1-2 HSFs).

Sequence Model / Sea Level	Depositional Sequence			Genetic Sequence	T-R Sequence	Coastal Plain-Fluvial Stage
References	Haq et al (1987)	Van Wagoner et al (1990)	Plint (2000)	Frazier (1974) Gallow (1989)	Curray (1964) Embry (1993,1995)	Pigott (2012)
High	HST	early HST	HST	HST	RST	HST
Rising	TST	TST	TST	TST	TST	TST
Low	late LST	LST	LST	late LST	RST	LST
Falling	early LST	late HST	FSST	early LST		RST
High	HST	early HST	HST	HST		HST

Table 7: Sequence models and their associated systems tracts. From Pigott et al. (2012).

In this investigation, the high-resolution sequence stratigraphic model used for this mixed siliciclastic-carbonate slope systems represented in Late Guadalupian outcrops is adapted from Pigott et al. (2012). Unlike the fully siliciclastic and fully carbonate depositional systems, the reciprocal sedimentation model of mixed siliciclastic-carbonate systems is in effect. Both the terrigenous siliciclastic supply and the in-situ carbonate supply are deposited along the slope in this depositional system. In the four systems tracts model (Table 7), the RST, LST, TST, and HST were defined by the attribution of relative

sea-level change in a complete cycle. The FSST was first fully defined by Plint (2000) and was interpreted as the symmetric complement to the TST, but renamed the RST by Pigott et al. (2012). During the RST, the sea level drops in stages in the mixed siliciclastic-carbonate environments in the study area.

Sequence Stratigraphic Framework			
Tinker (1998) and Kerans (2002)		This Study	
CS (3rd)	HFS (4th)	Sequence (4th)	HFCS
CS 14	G28 (T2)	T2	T2.2
			T2.1
	G27 (T1)	T1	T1.4
			T1.3
			T1.2
			T1.1
	G26 (Y6)	Y6	Y6.3
			Y6.2
			Y6.1
	G25 (Y5)	Y5	Y5.4
			Y5.3
			Y5.2
			Y5.1
CS 13	G24 (Y4)	Y4	Y4.4
			Y4.3

Table 8: Sequence stratigraphic framework of previous work and in this study.

The comparison of sequence stratigraphic terminology between this study and previous studies is listed in Table 8. In previous studies, high-frequency cycles (HFC), high-frequency sequences (HFSs), composite sequences (CSs), and super-sequences were defined from the smallest to largest units. The HFC is the smallest unit with the shortest time duration in a single base-level cycle. The cycle is analogous to a parasequence in Van Wagoner's terminology. Several HFCs in a same retrogradational, aggradational, or progradational pattern were named HFCS. HFSs, which are comparable to the fourth order sequences, are made up of HFCS (Kerans and Kempter 2002). In each

HFS, the systems tracts of lowstand, transgressive, and highstand in different stacking patterns are the major components. CSs are made up of high-frequency sequences, which are often equivalent to the third order depositional sequences. Both HFSs and CSs are bounded by subaerial unconformities and their correlative conformities (Kerans and Kempter, 2002). In this study, sequences are comparable to HFSs. To be noted, the labeling of the hierarchy of stratigraphic cycles in terms of orders (3^{rd}, 4^{th}, 5^{th}) has been downplayed in Kerans and Kempter's work because of the lack of rigorous chronologic analysis.

4.2.2 Lidar Sequence Boundaries

Beyond the application for accessing high-resolution spatial data, the LiDAR could also be utilized as a possible remote sensor of lithology, particularly in remote areas and inaccessible outcrops.

Intensity is the reflection energy of the laser pulse upon return to the laser scanner and is proportional to the reflectivity of the target outcrops. To minimize the impact of the laser energy decreases through long-distance travels and atmospheric conditions, a correction method was introduced for intensity data following the approach of Hofle and Pfeifer (2007). After laboratory experiments in clastic outcrops, Burton et al. (2011) illustrate a positive relationship between intensity and wt. % combined quartz, plagioclase, and K-feldspar. Giddens (2016) worked in a carbonate quarry and showed the high reflectance is associated with calcite-rich sections. In general, the reflectivity of carbonate sediments is higher than siliciclastic sediments.

In this study, the oversimplified lithology interpretation is conducted through 'reflectance view' in RISCAN software of the 3D LiDAR model. It is used to better

distinguish the strata terminations in company with ‘true color view’ where outcrops’ colors are extracted from high-quality images. The termination of downlap and onlap are well discussed in Chapter 3.2.3 based on the sequence stratigraphic glossary by Mitchum (1977). The reference work of the previous identification for stratigraphic units and terminations in foreslope sections were concluded by Brown (1993). These terminations are both observed in the field and identified through the rotatable LiDAR digital model which are more reliable than 2D plane images of previous studies.

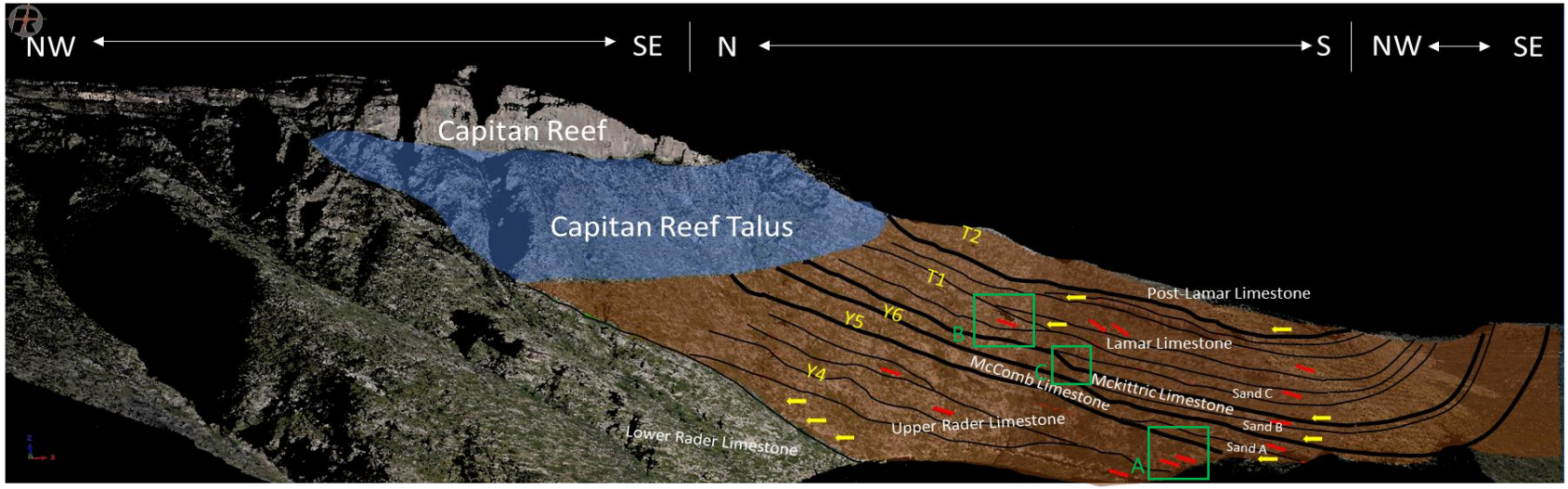

Figure 26: Interpretation of stratigraphic units and sequence units with Strata Termination shown in 'True Color' view. The three green squares highlighted the detailed sections shown below. Red arrows represent downlap and yellow arrows represent onlap.

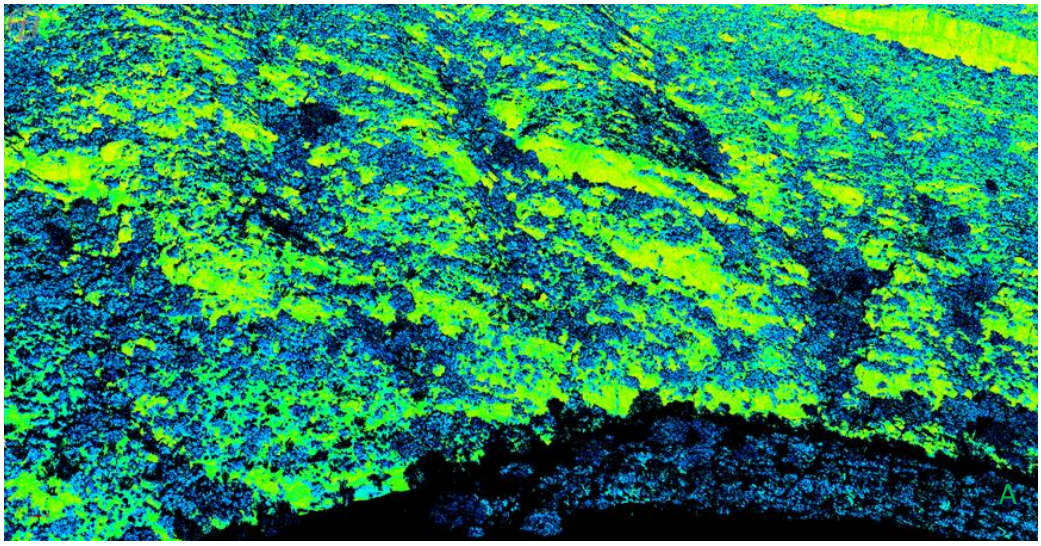

Figure 27: Detailed section in ‘Reflectance’ view of square A.

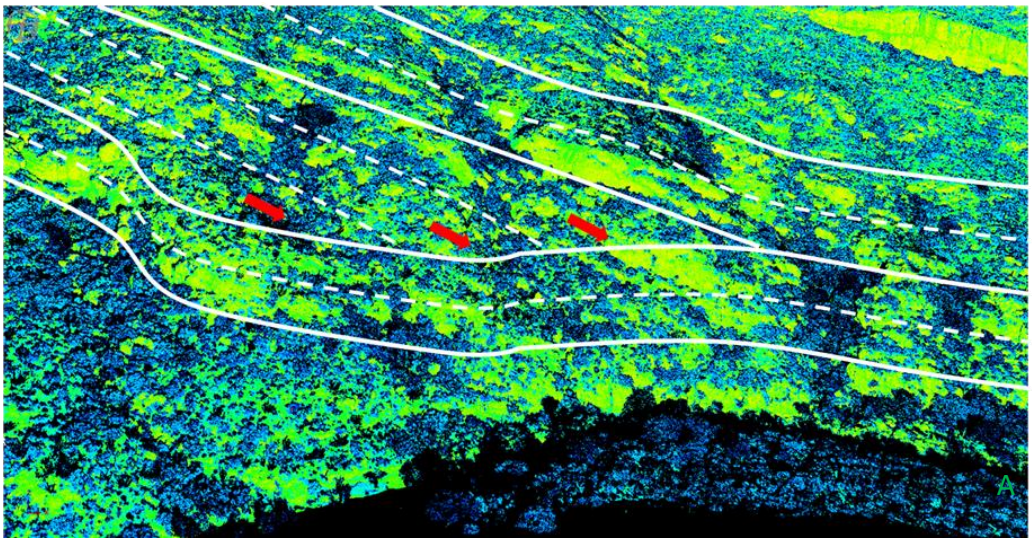

Figure 28: Detailed type 1 downlap identification in ‘Reflenctance’ view of square A. Shown in red arrows.

Figure 29: Detailed type 1 downlap identification in 'True Color' view of square A. Shown in red arrows

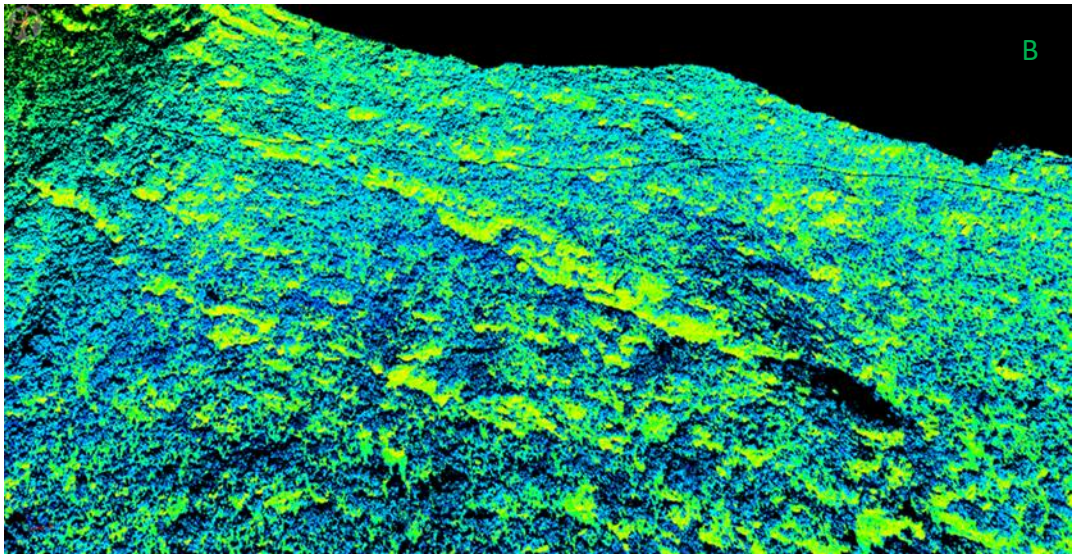

Figure 30: Detailed section in 'Reflectance' view of square B.

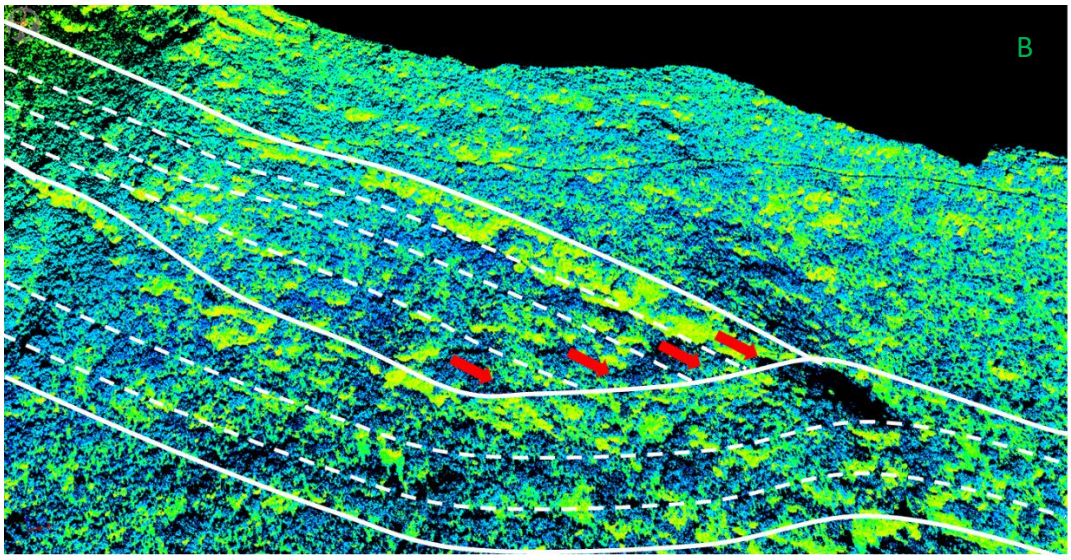

Figure 31: Detailed type 2 downlap identification in 'Reflectance' view of square B. Shown in red arrows.

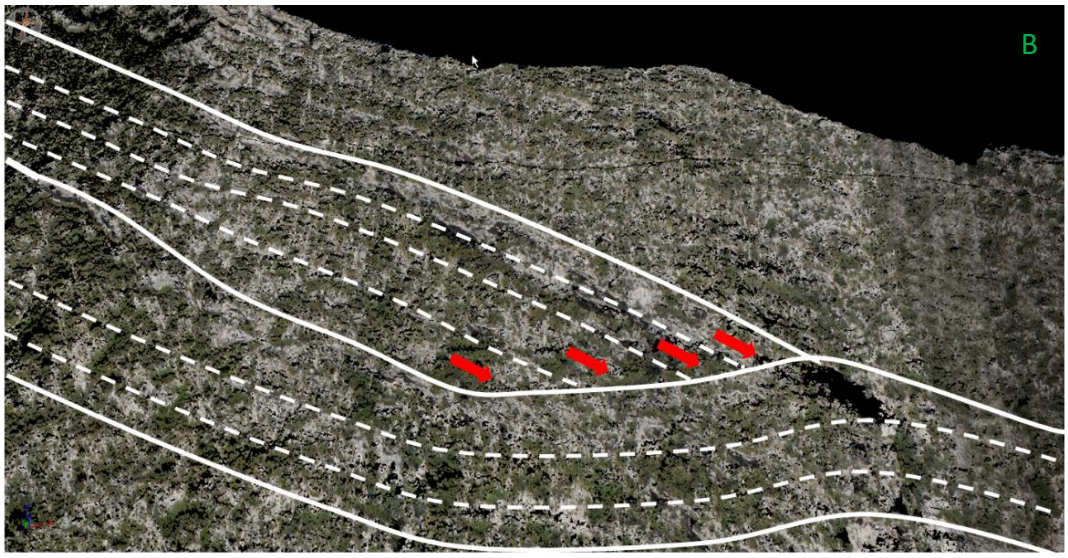

Figure 32: Detailed type 2 downlap identification in 'True Color' view of square B. Shown in red arrows.

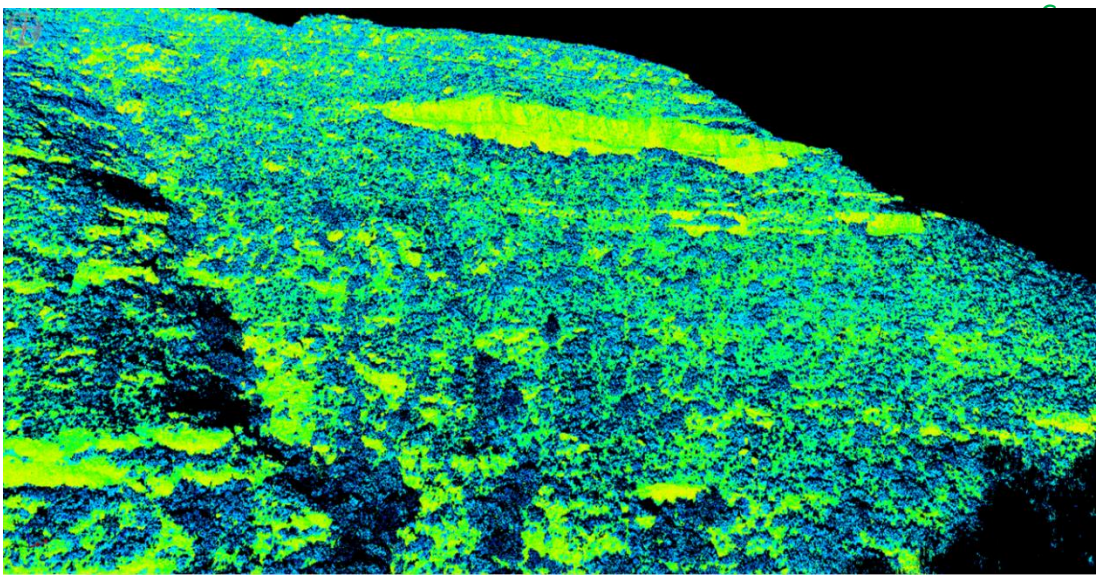

Figure 33: Detailed section in 'Reflectance' view of square C.

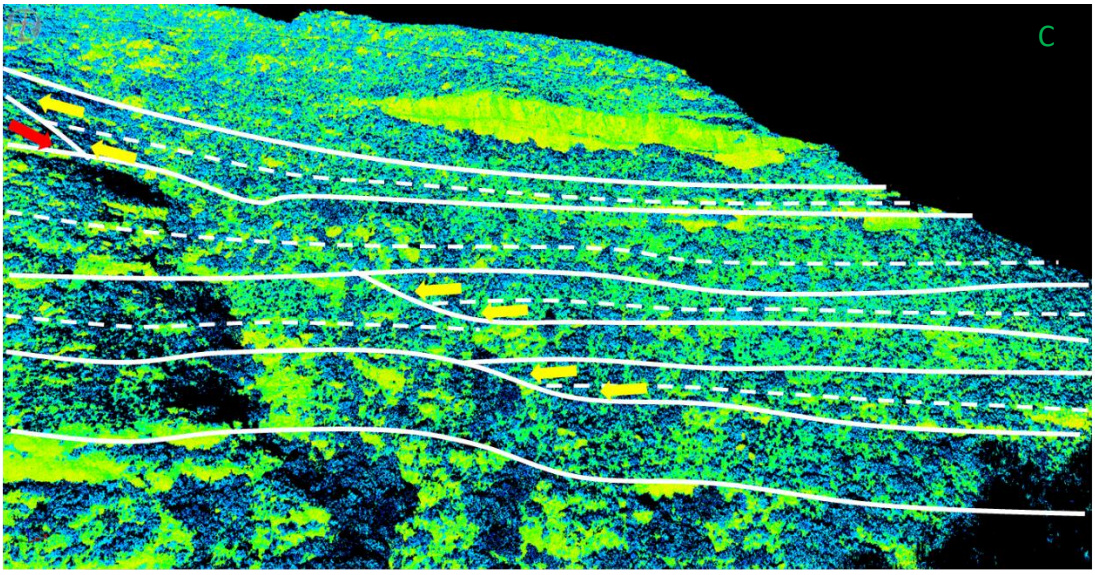

Figure 34: Detailed type 1 and type 2 onlap identification in 'Reflectance' view of square C. Shown in yellow arrows. Type 1 onlap are observed in toe-of-slope sections and type 2 onlap are observed in foreslope sections.

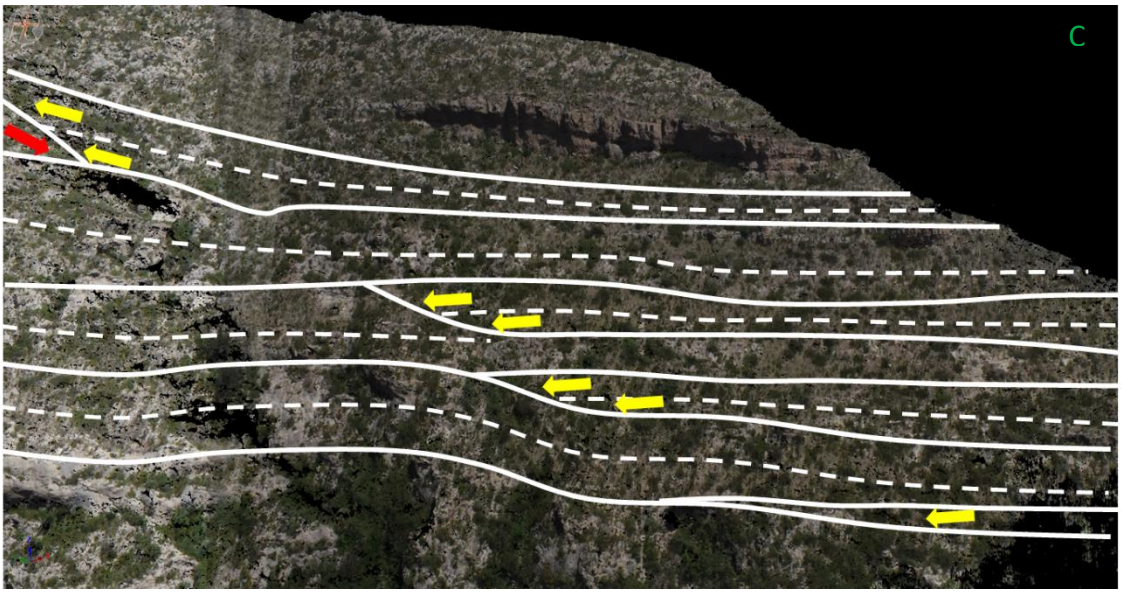

Figure 35: Detailed type 1 and type 2 onlap identification in 'True Color' view of square C. Shown in yellow arrows. Type 1 onlap are observed in toe-of-slope sections and type 2 onlap are observed in foreslope sections.

Generally, there appear to be two types of downlapping terminations in this study. Firstly, type 1 downlap occurs at the paleobathymetric highs on foreslope sections caused by paleogeometric variations (Figure 27; Figure 28; Figure 29). This is only a regional phenomenon and does not happen everywhere within the same strata. Secondly type 2 downlap occurs in strata characterized by matrix-poor or silty, conglomeratic deposits (Figure 30; Figure 31; Figure 32). These sediments from the upper slope to toe-of-slope are interpreted to be deposited by slope failure and debris flows. Following sediments come, the lower slope provides the base for the transportation of platform rocks and matrix-poor debris flows, but the toe-of-slope is not sufficient for continued transport according to the minimal dip angles. As a result, these sediments pinch out at the gently dipping toe-of-slope sections. For onlap, type 1 onlap occurs mainly in strata in toe-of-slope sections and is characterized by mixed siliciclastic-carbonate carbonates when the

terrigenous inputs are transported or incised into the slope during relatively low sea level. In addition, type 2 onlap is observed within mud-dominated carbonates on foreslope sections (Figure 33; Figure 34; Figure 35).

With respect to the relative sea-level variations and the observed geometric configurations of the different systems tracts within a complete fourth-order sequence, the shelfward onlapping strata are likely deposited during the LST and HST times. In contrast, the downlapping strata are deposited during RST, TST and HST. Details are concluded in Chapter 4.2.5.

4.2.3 Chemostratigraphy

Chemostratigraphy, or chemical stratigraphy, studies the variations of elements within sedimentary sequences and has been used for stratigraphic correlation (Tribovillard et al., 2005). In this study, chemostratigraphy is the main approach used to link stratigraphic units to provenance, paleoredox conditions, and relative sea level.

In this study, the chemostratigraphic analysis defines twelve chemostratigraphic packages that are common to both the foreslope sections and toe-of-slope sections. Each stratigraphic package is defined in terms of elemental variations in each proxy group along the XRF profile. (Figure 36; Figure 37). The characters for each chemostratigraphic package are listed in Table 9.

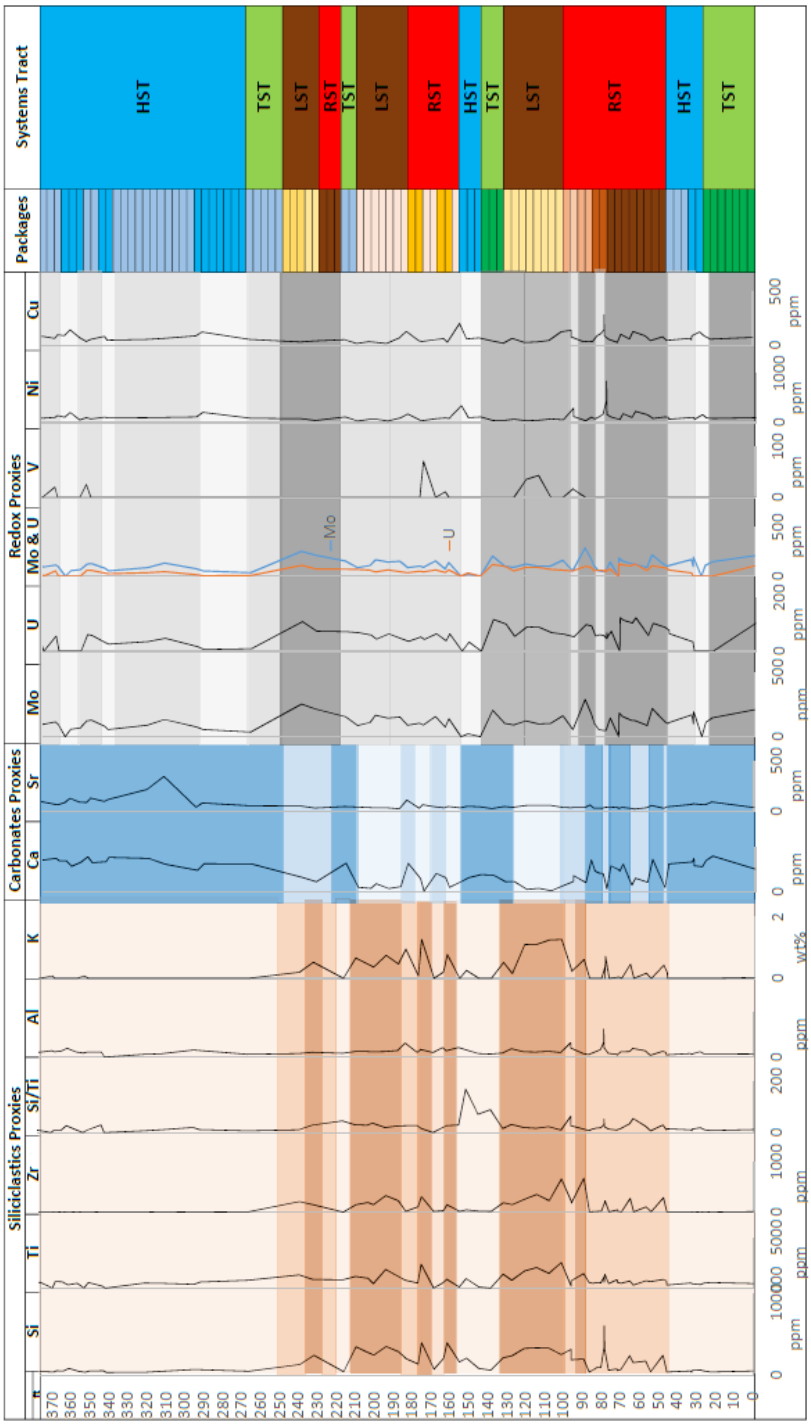

Figure 36: Chemostratigraphic packages interpretation in toe-of-slope sections. The colors in the Package column represent different identified chemostratigraphic packages.

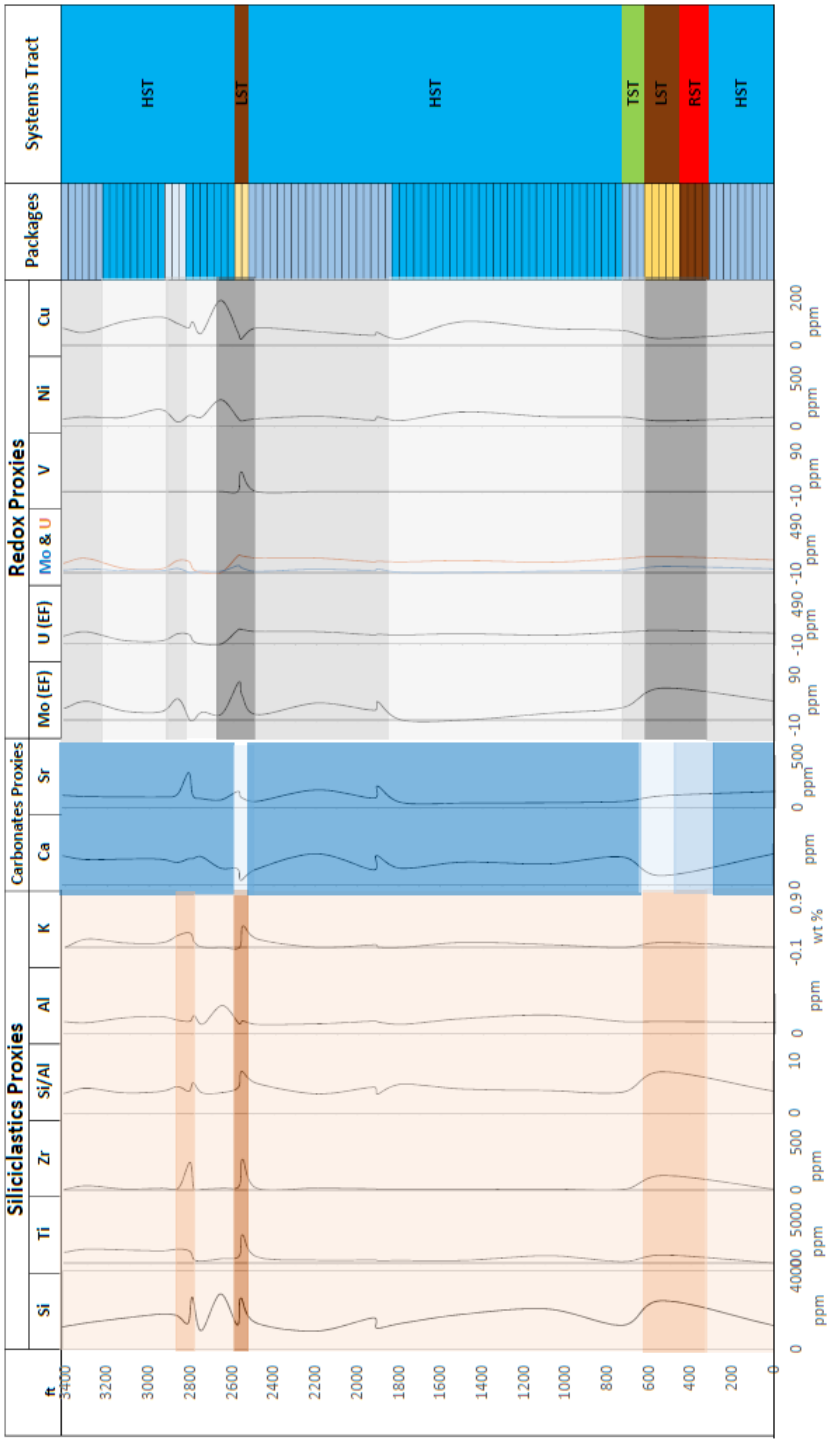

Figure 37: Chemostratigraphic packages interpretation in foreslope sections. The colors in the Package column represent different identified chemostratigraphic packages.

Chemostratigraphic Packages	Characters	Interpretation	System Tract Interpretation
Package 1	Moderate Si, Ti, Zr, K, Moderate to high Ca, High Mo, U	Siliciclastics-carbonates mixed sediments in shallow water	RST
Package 2	Low Ti, Zr, Moderate Ca, High Mo, U, Ni, Cu	Coarse-grained, matrix-poor carbonates in shallow water	RST
Package 3	High Ti, Zr, K, Moderate Ca, High Mo, U	Siliciclastics-carbonates mixed sediments in shallow water	RST
Package 4	High Ti, Zr, Moderate Ca, Moderate Mo, U	Siliciclastics-carbonates mixed sediments in relatively shallow water	RST
Package 5	High Si, Ti, Zr, K, low Si/ Ti, Low Ca, Moderate Mo, U	Fine-grained sandstone and siltstone in relative shallow water	RST/LST
Package 6	Moderate Ti, Zr, Moderate Ca, Moderate Mo, U	Siliciclastics-carbonates mixed sediments in relatively shallow water	RST
Package 7	High Si, Ti, Zr, K, Low Ca, High Mo, U	Fine-grained sandstone and siltstone in shallow water	LST
Package 8	Moderate Ti, Zr, Low Ca, High Mo, U	Fine-grained sandstone and siltstone in shallow water	LST
Package 9	Low Ti, Zr, moderate Si/Ti, High Ca, High Mo, U, low Ni, Cu	Coarse-grained, matrix-poor carbonates in relative deep water	TST
Package 10	Low Ti, Zr, High Ca, Low Mo, U, high Ni, Cu	Fine-grained, mud-dominated carbonates with organic matters in deep water	HST
Package 11	Low Ti, Zr, High Ca, Moderate Mo, U	Carbonates in relative deep water	TST/HST
Package 12	Moderate Ti, Zr, High Ca, Sr, Moderate Mo, U, low Ni, Cu	Coarse-grained, matrix-poor carbonates with little siliciclastics in relative deep water	TST

Table 9: Characteristics of twelve identified packages in terms of proxy variation. The descriptive term in the interpretation is not an absolute value but a relative descriptive term.

The Yates and Tansill time-equivalent formations located at the slope sections in Mckittrick Canyon were deposited in the Late Guadalupian, within a global second-order regression cycle during a time of regional relative dropping sea level. (Haq, 2008) The stratigraphic packages were therefore expected to be associated with sequence stratigraphy and sea level fluctuations. However, there are local variations.

The detailed elemental variations for different formations are discussed in Chapter 4.1.3 to Chapter 4.1.5. To link stratigraphic packages and systems tracts deposited during

different stages of sea level alteration, the provenance-responded siliciclastic proxies and carbonate proxies were firstly used to analyze the shoreline trajectory. After applying the hierarchical cluster analysis discussed in Chapter 4.1.2, selected siliciclastic proxies (such as Ti, Zr, K) and carbonate proxies (Ca, Sr) are expected to be significantly associated with marine transgression and regression (Turner, 2016). As the siliciclastic proxies increase and carbonate proxies decrease in concentration, the relative sea level drops and the shoreline moves basinward. Because during these stages, the pre-exiting shelf margin is likely subaerially exposed and the detrital sediments bypassed the platform rim. At the same time, the carbonate sediments decrease as a result of the termination of the shelfal carbonate mud factory. When the siliciclastic proxies decrease and carbonate proxies increase in concentration, it implies the relative sea level rises and the shoreline moves landward with an increase in carbonate platform productivity. Consequently, the carbonate deposits accumulated on foreslope and fewer siliciclastics on siliciclastics are deposited.

Redox proxies (such as Mo, V, U) were employed to analyze the bottom water circulation within the different systems tracts. The relatively high values are linked to suboxic to anoxic environments, and moderate to low values are linked to oxic to suboxic environments. The interpreted characteristics of these packages and associated sequence events are listed in Table 4.6 and Table 4.7.

System Tracts	Start Time	End Time	Elemental Characters			Packages
			Siliciclastic Proxies	Carbonate Proxies	Redox Proxies	
HST	End of Transgression	End of HST Stasis	Low	High	Low to Moderate	10, 11
RST	End of HST Stasis	End of Base-Level Fall	Moderate to High	Low to Moderate	Moderate to High	1, 2, 3, 4, 5, 6
LST	End of Base-Level Fall	End of LST Stasis	Moderate to High	Low	High	5, 7, 8
TST	End of LST Stasis	End of Transgression	Moderate	Moderate to High	Moderate to High	9, 11, 12

Table 10: The start and end times of systems tracts and associated proxy variations in this study.

4.2.4 Sequence Stratigraphic Frameworks

The data used to establish the two high-resolution sequence stratigraphic frameworks for the late Guadalupian slope include outcrop observations, XRF data, and the 3D digital LiDAR model in McKittrick Canyon. The frameworks are built according to the pseudo gamma ray interpretations, LiDAR sequence boundary identifications, and chemostratigraphic interpretations. In the study areas, the Late Guadalupian succession comprises five fourth-order sequences, fifteen high-frequency cycle sets, and twenty possible fifth-order high-frequency cycles.

Two high-resolution sequence stratigraphic frameworks are shown in Figure 38 and Figure 39. Blue vertical arrows represent HSTs; Red arrows pointing to the right represent RSTs; Brown vertical arrows represent LSTs; Green arrows pointing to the left represent TSTs.

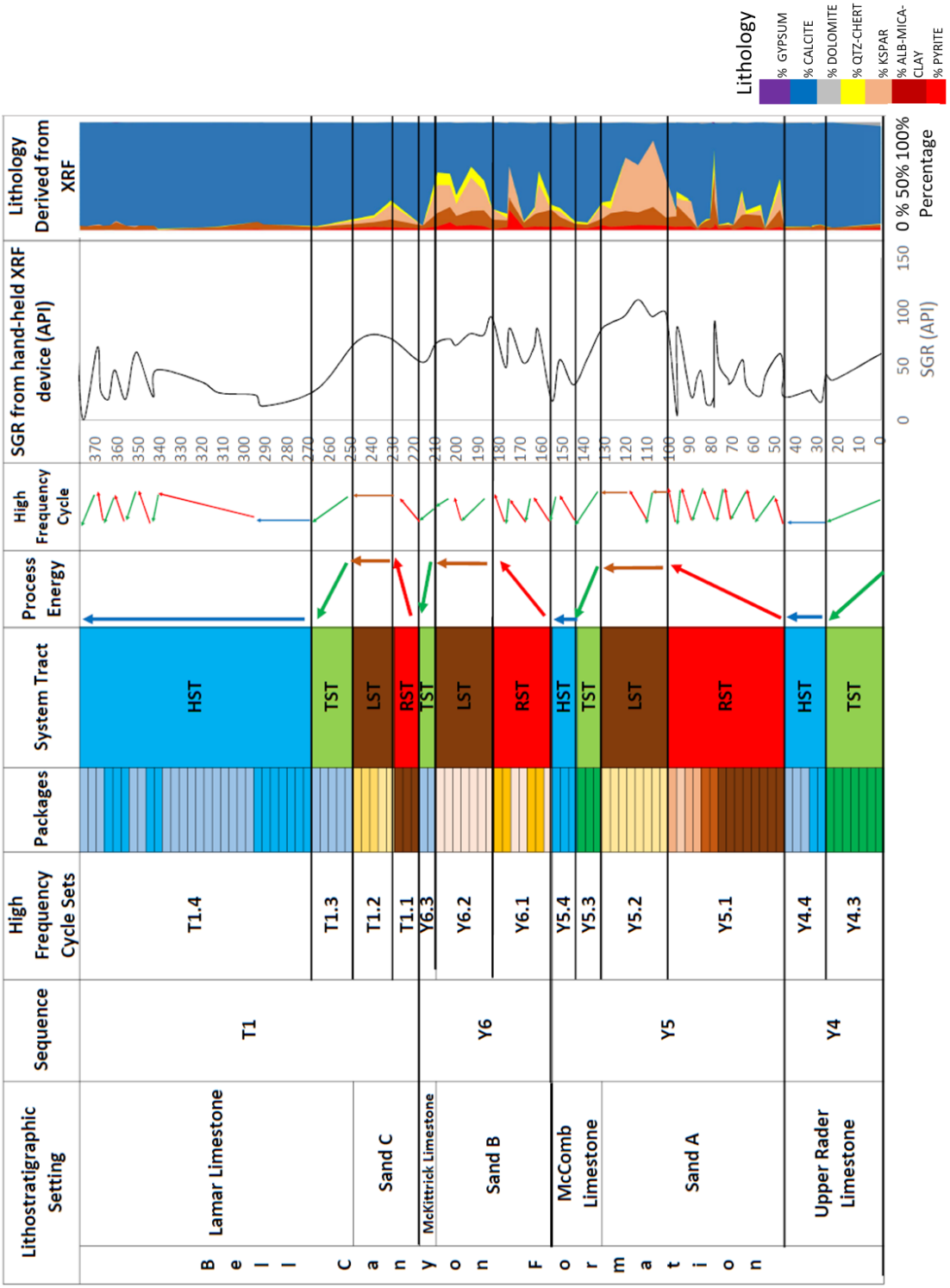

Figure 38: Sequence stratigraphy framework of toe-of-slope section.

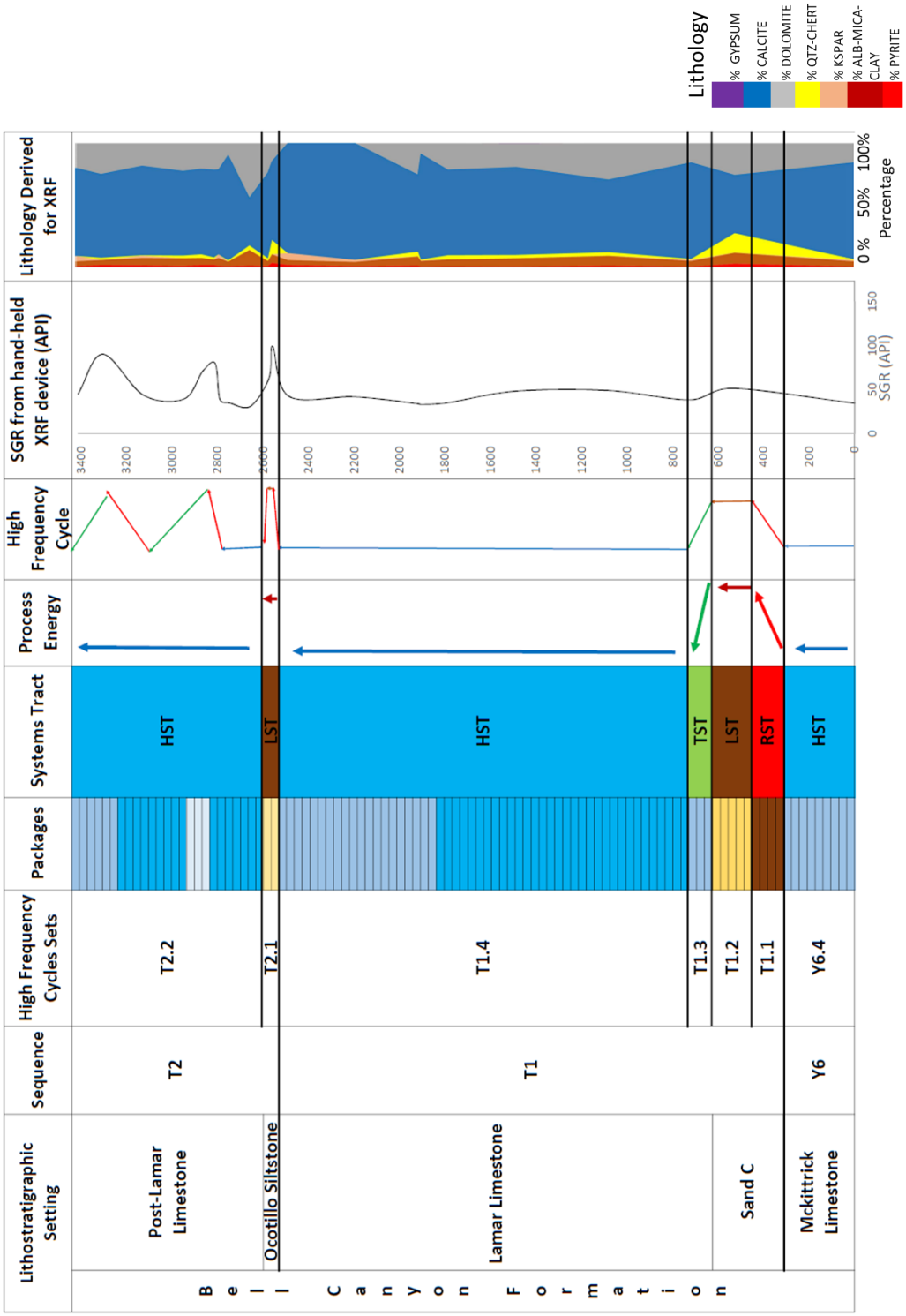

Figure 39: Sequence stratigraphy framework of foreslope sections.

The cycles observed at the slope in McKittrick Canyon are believed to represent true sequences bounded by Vail's unconformities and can be further subdivided into smaller cycles (Brown, 1993). The sequence boundaries are recognized in terms of outcrop observations, LiDAR sequence boundary interpretations, and responses of XRF elemental proxies. The toe-of-slope sections show greater distinctions that make sequence boundaries more easily identified whereas fewer distinctions are observed on mostly carbonate covered foreslopes. At the bottom of measured sections measured in the study areas is the Upper Rader Member. A sequence boundary between Y4 and Y5 is interpreted on top of it based on correlation with the subaerial exposure surface of Corral Carbonate observed in the field. In addition, the shift in elemental proxies and pseudo gamma ray logs confirme its existence. Y4 is subdivided into two HFCS (Y4.3-TST and Y4.4-HST) according to the alteration from more reducing environments to more oxidizing environments based on variations of redox proxies. The upper HSCS is also observed to be less radioactive. It indicates the trend of better water mass circulation and decreasing siliciclastics inputs as the result of rising sea level. In Y5, the Sand A unit is named for the thick lowstand deposits which onlap foreslope equivalent of the Upper Rader Member. The boundary between the regressive deposits and the lowstand deposits can be interpreted from the elemental proxies. In Y5, two more HFCS are recognized within carbonate deposits of the McComb Limestone. The sequence boundary between Y5 and Y6 and Y6 and T1 are subaerial exposure unconformities observed in the field. There are three HFCS identified in Y6 and four HFCS identified in T1. The HFCS (Y6.3 - TST) which includes most of McKittrick Limestone has its lower boundary on top of the Sand B unit deposited as Y6.1 (RST) and Y6.2 (LST). In T1, there are four HFCS

interpreted within the Sand C unit and Lamar Limestone with the help of previous interpretation of elemental proxies and pseudo gamma ray characteristics. T2 is only observed in the post-Lamar Member at the lower slopes. Though some of the section has been removed by long-term subaerial exposure, two HFCS are identified. The T2.1 HFCS is characterized by the lowstand deposits of the Ocotillo silts and T2.2 mainly includes the Upper Tansill Carbonate deposited at relatively high sea level.

4.2.5 Sequence Depositional Settings

In this mixed siliciclastic-carbonate slope system, variations of relative sea level are significant factors affecting depositional settings in terms of sediment supplies and depositional locations. Based on the sediment provenance analysis discussed in Chapter 4.1.3 and 3D LiDAR observations associated with sea level interpretations discussed in Chapter 4.2.2, the different depositional settings of a complete sequence within different systems tracts are summarized below:

LST: Relative sea level starts to rise but sedimentation rates are greater than rates of relative sea level rise. Normal regression occurs within this systems tract. The aggradation of mostly siliciclastics with small amounts of coarse carbonates happening from the toe-of-slope sections to the basin is the most common strata stacking pattern (Figure 40). The fine-grained siliciclastics are transported from shelf or winds.

TST: The rates of relative sea level rising outpace the sedimentation rates and transgression occurs within this systems tract. Reefs start to grow but the shelf carbonate mudstone factory is still inactive. The siliciclastic inputs are constrained according to the reef barriers on the shelf margin. Coarse-grained, matrix-poor

sediments caused by the slope failures form the thick and steeply dipping beds at the foreslopes and pinch out with downlapping terminations on gently dipping toe-of-slope sections (Figure 41).

HST: Relative sea level is about to drop to a slower rate from the highest position. The siliciclastic sediments during this stage are negligible. Fine-grained, mud-dominated carbonates exhibit aggradation and progradation on foreslope and toe-of-slope sections. The deposits develop onlapping terminations against the preexisted beds. The shoreline continues to move basinwards during this stage, the shelves are flooded and the reef boundstone debris are deposited at forslopes, forming the downlapping termination (Figure 42).

RST: Relative sea level drops quickly and the shelf margin starts to be subaerially exposed. Forced regression occurs within this systems tract. Siliciclastics are transported across the shelf and bypass or incise foreslopes and are accumulated at foreslope and toe-of-slopes places. With the rapid relative sea level dropping rate, the massive reef growth ceases and the carbonate mud factory on the shelf is shut down. Coarse grained, matrix poor mixed siliciclastic-carbonate sediments are deposited along the slope (Figure 43).

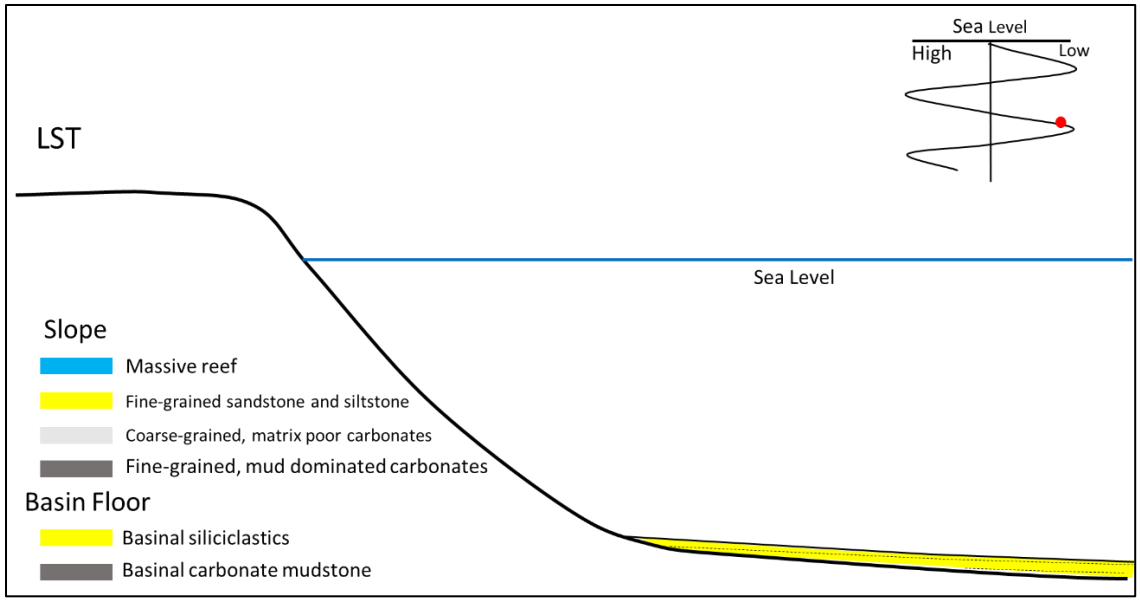

Figure 40: Slope developments during LST stage.

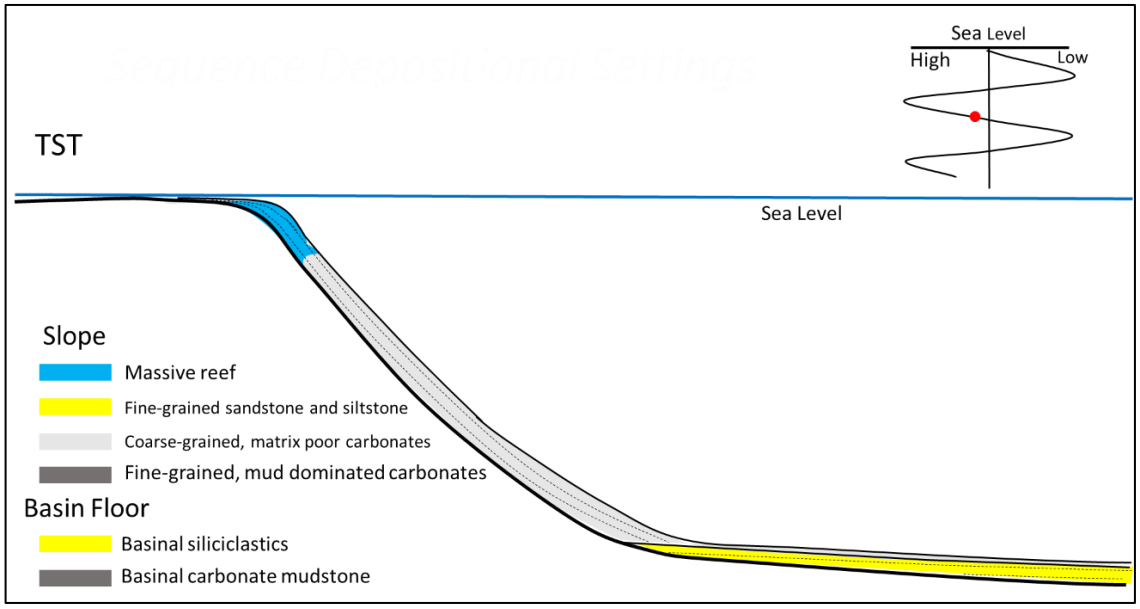

Figure 41: Slope developments during TST stage.

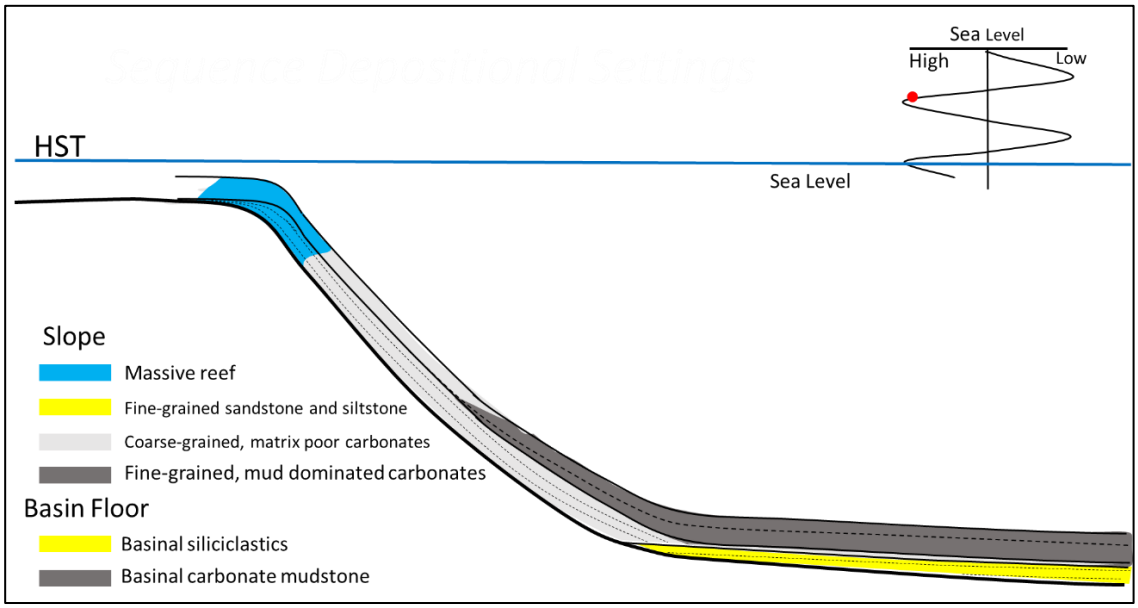

Figure 43: Slope developments during HST stage.

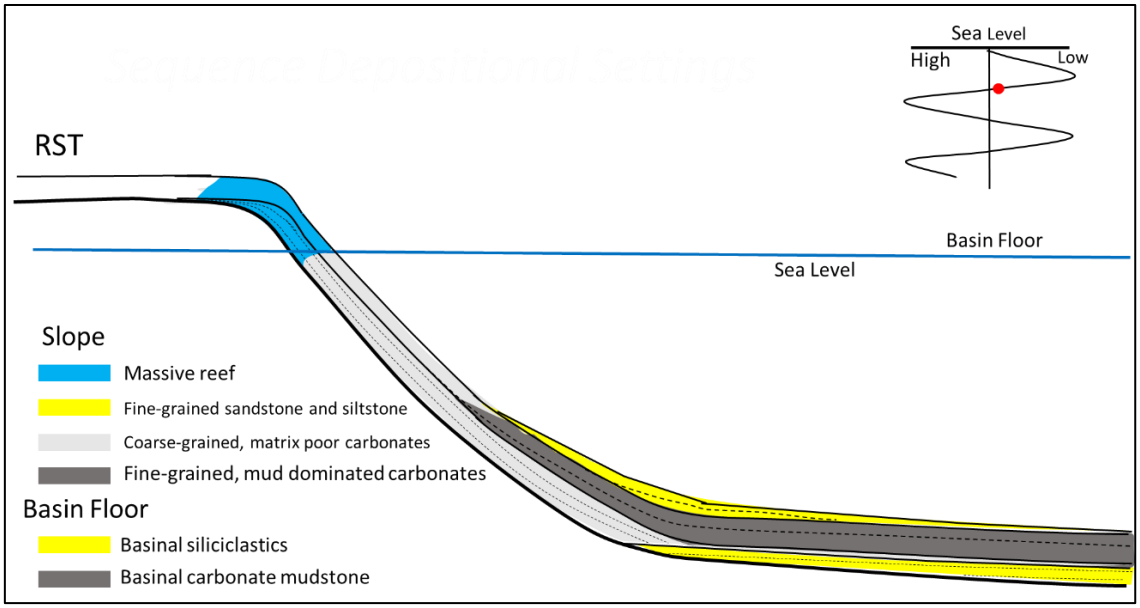

Figure 42: Slope developments during RST stage.

4.2.6 Sea Level Variations

Throughout Earth history, sea level has changed at different magnitudes and time. In sequence stratigraphy, paleo global sea level changes are cyclic phenomena and are able to be described into five different orders. With Frequencies. Sea levels are

superimposed on one another to form a complex sea level curve. Generally, a third-order sequence is a composite of fourth- and fifth-order sequences. In Figure 44, both long-term second-order cycles and short-term third-order cycles are shown by Haq and Schutter (2008). These fluctuations are displayed in the left column of Figure 44. The fourth- and fifth- order cycles of fluctuations in sea level in the same geological stages from the pseudo gamma ray logs in this research are displayed in the right column. The possible twenty fifth-order cycles here are still questionable and needed to be coupled with other data to support. The reconstruction of the local sea level changes associated with such high frequency is meaningful as a reference for future geological analysis. Differences between the observed cycles and those of the global curve of Haq and Schutter (2008) are likely due to local differences in the Delaware Basin as the Hovey Channel opens and close (Crosby, 2015).

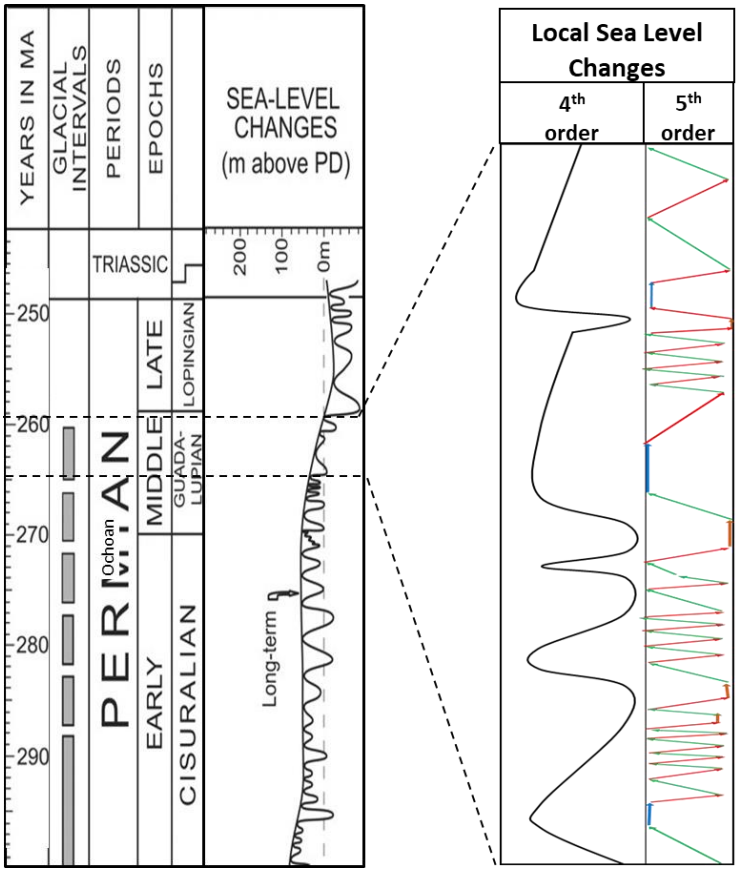

Figure 44: Changes of 4th and 5th order sea level cycles derived from this research correlated to the global sea level curve for the Permian from Haq and Schutter (2008). Long-term 2nd cycles and short-term 3rd sea level cycles of Haq and Schutter (2008) are shown in left column. The high-resolution 4th and 5th order cycles derived from the pseudo gamma ray logs are shown in right column.

Chapter 5 Conclusion

1. A high-resolution sequence stratigraphic framework along two measured sections on the slope in McKittrick Canyon of the Guadalupe Mountains is established. Five fourth-order sequences, fifteen high-frequency cycles sets, and twenty possible high-frequency cycles are identified based on outcrop observations, XRF data, and the 3D digital LiDAR model.

2. In the study area, pseudo gamma ray logs calculated from Th, U, and K detected by hand-held X-ray Fluorescence Analyzer proved to be a good tool to use when no gamma ray data are available. The high pseudo gamma ray values are more associated with siliciclastic units and low pseudo gamma ray values are associated with carbonate units. This characteristic of pseudo gamma rays in the mixed siliciclastic-carbonate systems allows researchers to distinguish lithologies between siliciclastics and carbonates and interpret sequence boundaries

3. Twelve chemostratigraphic packages were defined based on the variations of elemental proxies determined from hierarchical cluster analysis. The changes of elemental proxies are interpreted to be significantly influenced by the sea level changes.

4. LiDAR is a reliable outcrop observation technique to identify bedding terminations. Two types of onlap and downlap were observed in this study. Considered with the relative sea-level variations and configurations of different systems tract within a complete fourth-order sequence, the onlap termination is observed in LST and HST, whereas the downlap termination is observed in RST, TST and HST.

5. The foreslopes were mostly developed under oxic to suboxic environments whereas toe-of-slope sections were mostly developed under suboxic to anoxic environments. The redox conditions were mainly associated with water renewal circulations caused by relative sea level changes. During the low sea level periods, the influx of marine-derived water from the Panthalassa Ocean was less. The water mass circulation only occurred at the top of water. During the high sea level periods, the Hovey Channel became larger and deeper. The well water circulation brought more dissolved oxygen from water of Panthalassa Ocean.

6. In the development of mixed siliciclastic-carbonate slope systems, relative sea level is an important factor affecting depositional settings in terms of sediment supplies and depositional locations. The ideal sequence depositional model was established. During relatively low sea level, the fine-grained siliciclastics mixed with coarse-grained carbonates were produces by shelf exposure and deposition on the slope. During relatively high sea level, the sediments of mostly mud-dominated carbonates and fewer siliciclastics were deposited on slope.

References

Adams, J. E. ,1965, Stratigraphic-tectonic development of Delaware Basin. AAPG Bulletin, 49(11), 2140-2148.

Algeo, T. J., & Rowe, H., 2012, Paleoceanographic applications of trace-metal concentration data. Chemical Geology, 324, 6-18.

Algeo, T. J., & Tribovillard, N., 2009, Environmental analysis of paleoceanographic systems based on molybdenum–uranium covariation. Chemical Geology, 268(3-4), 211-225.

Bahr, A., Lamy, F., Arz, H. W., Major, C., Kwiecien, O., & Wefer, G., 2008, Abrupt changes of temperature and water chemistry in the late Pleistocene and early Holocene Black Sea. Geochemistry, Geophysics, Geosystems, 9(1).

Beaubouef, R., Rossen, C., Zelt, F., Sullivan, M., Mohrig, D., & Jennette, D., 1999, Field guide for AAPG Hedbergfield research conference-April 15–20, 1999: Deep-water sandstones, Brushy Canyon Formation, West Texas. Continuing Education Course Note Series, 40.

Bebout, D. G., & Kerans, C., 1993, Guide to the Permian Reef Geology Trail, McKittrick Canyon, Guadalupe Mountains National Park, West Texas: Bureau of Economic Geology, University of Texas at Austin.

Booler, J., & Tucker, M. E., 2002, Distribution and geometry of facies and early diagenesis: the key to accommodation space variation and sequence stratigraphy: Upper Cretaceous Congost Carbonate platform, Spanish Pyrenees. Sedimentary Geology, 146(3-4), 225-247.

Borer, J., & Harris, P., 1991, Lithofacies and Cyclicity of the Yates Formation, Permian Basin: Implications for Reservoir Heterogeneity (1). AAPG Bulletin, 75(4), 726-779.

Borer, J., & Harris, P. M., 1995, Computer simulation of the Yates Formation (Permian, Delaware Basin)—Sequence stratigraphy and shelf-to-basin correlation implications. In Search of New Permian Oil and Gas Fields: Using Today's Technologies and Tomorrow's Ideas for Exploration, Development and 3D Seismic in a Mature Basin: West Texas Geological Society, Publication, 95-98.

Brown, A., & Loucks, R., 1993, Influence of Sediment Type and Depositional Processes on Stratal Patterns in the Permian Basin-Margin Lamar Limestone, McKittrick Canyon, Texas: Chapter 5.

Brumsack, H.-J., 1989, Geochemistry of recent TOC-rich sediments from the Gulf of California and the Black Sea. Geologische Rundschau, 78(3), 851-882.

Buckley, S. J., Schwarz, E., Terlaky, V., & Howell, J. A., 2010, Combining aerial photogrammetry and terrestrial lidar for reservoir analog modeling. Photogrammetric Engineering & Remote Sensing, 76(8), 953-963.

Burton, S., Ferrare, R., Hostetler, C., Hair, J., Rogers, R., Obland, M., . . . Froyd, K., 2012, Aerosol classification using airborne High Spectral Resolution Lidar measurements-methodology and examples. Atmospheric Measurement Techniques, 5(1), 73.

Calvert, S., & Pedersen, T., 1993, Geochemistry of recent oxic and anoxic marine sediments: implications for the geological record. Marine geology, 113(1-2), 67-88.

Catuneanu, O., 2002, Sequence stratigraphy of clastic systems: concepts, merits, and pitfalls. Journal of African Earth Sciences, 35(1), 1-43.

Cook, H. E., Hine, A. C., & Mullins, H. T., 1983, Platform margin and deep water carbonates: Citeseer.

Crosby, C.B., 2015, Depositional History and High Resolution Sequence Stratigraphy of the Leonardian Bone Spring Formation, Northern Delaware Basin, Eddy and Lea Counties, New Mexico: Master's thesis, University of Oklahoma, p. 1-230.

Doveton, J., & Merriam, D., 2004, Borehole petrophysical chemostratigraphy of Pennsylvanian black shales in the Kansas subsurface. Chemical Geology, 206(3-4), 249-258.

Dunham, R. J., 1972, Capitan Reef, New Mexico and Texas: facts and questions to aid interpretation and group discussion (Vol. 72): Permian Basin Section, Society of Economic Paleontologists and Mineralogists.

Esteban, M., & Pray, L., 1977, Origin of the pisolite facies of the shelf crest. Paper presented at the Upper Guadalupian Facies, Permian Reef Complex, Guadalupe Mountains, New Mexico and West Texas: SEPM, Permian Basin Section, Field Conference Guidebook, Publication.

Fagerstrom, J. A., & Weidlich, O., 1999, Strengths abd weaknesses of the reef guild concepts and quantitative data: Application to the upper Capitan-massive community (Permian), Guadalupe Mountains, New Mexico-Texas. Facies, 40(1), 131.

Fiedler, A. G., & Nye, S. S, 1933, Geology and ground-water resources of the Roswell artesian basin, New Mexico. Retrieved from

Garrett, K. N., 2015, High Resolution Basin Modeling of the Permian Capitan Reef, New Mexico: New Insight from Integrated Outcrop LiDAR-XRF-SGR Analysis Into Reef Architecture. University of Oklahoma.

Garrett, K. N., Pigott, J. D., & Pigott, K. L., 2018, High Resolution Basin Modeling Insight Into Syndepositional Permian Reef Architecture Through Integrated Lidar-XRF Analysis, Slaughter Canyon, New Mexico. Paper presented at the AAPG Annual Convention and Exhibition.

Geogory, P. W., David M. O., and Govert J.B., 2013, Calcisponge-microbialite(lower Guadalupian), northwest shelf margin of Permian Basin, New Mexico: AAPG Bulletin, v. 97, No.11, p. 1895-1897.

Giddens, E., Pigott, J. D., & Pigott, K. L., 2016, Pleistocene Coral Reef Destruction in the Florida Keys: Paleotempestite Evidence from a High Resolution LIDAR XRF Analysis of Windley Key Quarry. Sea, 100, 120.

Hampson, G. J., Davies, W., Davies, S. J., Howell, J. A., & Adamson, K. R, 2005, Use of spectral gamma-ray data to refine subsurface fluvial stratigraphy: Late Cretaceous strata in the Book Cliffs, Utah, USA. Journal of the Geological Society, 162(4), 603-621.

Handford, C. R., & Loucks, R. G., 1993, Carbonate Depositional Sequences and Systems Tracts--Responses of Carbonate Platforms to Relative Sea-Level Changes: Chapter 1.

Haq, B. U., & Schutter, S. R., 2008, A chronology of Paleozoic sea-level changes. Science, 322(5898), 64-68.

Hernon, R. M., Jones, W. R., & Moore, S., 1953, Some geological features of the Santa Rita quadrangle, New Mexico. Paper presented at the New Mexico Geological Society Guidebook, 4th Field Conference, Southwestern New Mexico.

Hills, J. M., 1984, Sedimentation, tectonism, and hydrocarbon generation in Delaware basin, west Texas and southeastern New Mexico. AAPG Bulletin, 68(3), 250-267.

Hill, C. A., 1996b, Guadalupian Series, in C. A. Hill, ed., Geology of the Delaware Basin, Guadalupe, Apache, and Glass Mountains, New Mexico and West Texas: SEPM Special Publication 96-39, p. 60-69.

Hodell, D. A., Channell, J. E., Curtis, J. H., Romero, O. E., & Röhl, U., 2008, Onset of "Hudson Strait" Heinrich events in the eastern North Atlantic at the end of the middle Pleistocene transition (~ 640 ka)? Paleoceanography, 23(4).

Höfle, B., & Pfeifer, N., 2007, Correction of laser scanning intensity data: Data and model-driven approaches. ISPRS journal of photogrammetry and remote sensing, 62(6), 415-433.

Horak, R., 1985, Tectonic and hydrocarbon maturation history in the Permian Basin. Oil & Gas Journal, 83(21), 124-129.

Kerans, C., Harris, P., & Bebout, D., 1993, Outer shelf and shelf crest. Guide to the Permian Reef Geology Trail, McKittrick Canyon, Guadalupe Mountains National Park, West Texas: University of Texas, Bureau of Economic Geology, Guidebook, 26, 32-43.

Kerans, C., & Kempter, K., 2002, Hierarchical stratigraphic analysis of a carbonate platform. Permian of the Guadalupe Mountains [CD-ROM]: AAPG (American Association of Petroleum Geologists)/Datapages Discovery Series, 5.

Kerans, C., Kempter, K., Rush, J., & Fisher, W., 2000, Facies and stratigraphic controls on a coastal paleokarst, Lower Permian, Apache Canyon, west Texas. PUBLICATIONS-WEST TEXAS GEOLOGICAL SOCIETY, 55-81.

Kerans, C., & Tinker, S. W., 1997, Sequence stratigraphy and characterization of carbonate reservoirs (Vol. 40): SEPM.

King, P. B., 1942, Permian of West Texas and Southeastern New Mexico: PART 1. AAPG Bulletin, 26(4), 535-763b.

King, P. B., 1948, Geology of the southern Guadalupe Mountains, Texas (Vol. 215): US Government Printing Office.

Krassay, A., 1998. Outcrop and drill core gamma-ray logging integrated with sequence stratigraphy: examples from Proterozoic sedimentary successions of northern Australia. AGSO Journal of Australian Geology and Geophysics, 17, 285-300.

Lefsky, M. A., & McHale, M. R., 2008, Volume estimates of trees with complex architecture from terrestrial laser scanning. Journal of Applied Remote Sensing, 2(1), 023521.

Lew, C., Baharuddin, S., & Pigott, J., 2013, Deepwater Basin Model for the Permian: Delaware Basin Example. Paper presented at the IPTC 2013: International Petroleum Technology Conference.

Mazzullo, S., 1981, Facies and burial diagenesis of a carbonate reservoir: Chapman Deep (Atoka) field, Delaware Basin, Texas. AAPG Bulletin, 65(5), 850-865.

McLennan, S. M., 2001, Relationships between the trace element composition of sedimentary rocks and upper continental crust. Geochemistry, Geophysics, Geosystems, 2(4).

Meissner, F. F., 1972, Cyclic sedimentation in Middle Permian strata of the Permian basin, west Texas and New Mexico. Cyclic sedimentation in the Permian Basin, 203-232.

Mitchum Jr, R, 1977, Seismic stratigraphy and global changes of sea level: Part 11. Glossary of terms used in seismic stratigraphy: Section 2. Application of seismic reflection configuration to stratigraphic interpretation.

Mitchum Jr, R. M., & Van Wagoner, J. C., 1991, High-frequency sequences and their stacking patterns: sequence-stratigraphic evidence of high-frequency eustatic cycles. Sedimentary Geology, 70(2-4), 131-160.

Morford, J. L., & Emerson, S., 1999, The geochemistry of redox sensitive trace metals in sediments. Geochimica et Cosmochimica Acta, 63(11-12), 1735-1750.

Nance, H. S., & Rowe, H., 2015, Eustatic controls on stratigraphy, chemostratigraphy, and water mass evolution preserved in a Lower Permian mudrock succession, Delaware Basin, west Texas, USA. Interpretation, 3(1), SH11-SH25.

Oskin, M. E., Arrowsmith, J. R., Corona, A. H., Elliott, A. J., Fletcher, J. M., Fielding, E. J. Liu-Zeng, J., 2012, Near-field deformation from the El Mayor–Cucapah earthquake revealed by differential LIDAR. Science, 335(6069), 702-705.

Osleger, D. A., 1998, Sequence architecture and sea-level dynamics of Upper Permian shelfal facies, Guadalupe Mountains, southern New Mexico. Journal of Sedimentary Research, 68(2).

Osleger, D. A., & Tinker, S. W., 1999, Three-dimensional architecture of Upper Permian high-frequency sequences, Yates-Capitan shelf margin, Permian Basin, USA.

Pigott, John D., Zhai, Rui, Pigott, Kulwadee L., and Tonianse, T., 2012, Searching for the Missing Link: The Regressive System Tract – Seismic Stratigraphic Evidence from the Southern Gulf of Thailand, International Petroleum Technology Conference, Bangkok, Thailand IPTC 1511-PP, 21pp.

Pigott, John D., Michael T. Williams, Mohamed Abdel-Fattah, and Kulwadee L. Pigott., 2014, The Messinian Mediterranean Crisis: A Model for the Permian Delaware Basin? AAPG International Conference & Exhibition, 14-17 September, 2014, Istanbul.

Pigott, John D., Esra Yalcin, Kulwadee L. Pigott, and Michael Williams., 2015, 3D Delaware basin model: Insight into its heterogeneous petroleum system evolution

as a guide to new exploration, West Texas Geological Society Convention, Midland, Tx

Pigott, John D., Kulwadee L. Pigott, Esra Yalcin, and Michael Williams., 2016, 3D Delaware Basin Petroleum System Evolution: Solution of the Basin Inverse Boundary Value Problem, Hedberg Conference: The Future of Basin and Petroleum Systems Modeling, 3-8 April 2016, Santa Barbara , CA, USA.

Pigott, K. L., 2004, Elemental and stable carbon isotope chemostratigraphy of the Upper Jurassic Smackover sequence of southwest Alabama basins, Alabama, United States.

Piper, D., & Perkins, R., 2004, A modern vs. Permian black shale—the hydrography, primary productivity, and water-column chemistry of deposition. Chemical Geology, 206(3-4), 177-197.

Playton, T., 2008, Characterization, variations, and controls of reef-rimmed carbonate foreslopes.

Plint, A. G., & Nummedal, D., 2000, The falling stage systems tract: recognition and importance in sequence stratigraphic analysis. Geological Society, London, Special Publications, 172(1), 1-17.

Pope, M., & Read, J. F., 1998, Ordovician metre-scale cycles: implications for climate and eustatic fluctuations in the central Appalachians during a global greenhouse, non-glacial to glacial transition. Palaeogeography, Palaeoclimatology, Palaeoecology, 138(1-4), 27-42.

Pringle, J., Gardiner, A., & Westerman, R., 2004, Topics: Virtual geological outcrops–fieldwork and analysis made less exhaustive? Geology Today, 20(2), 67-71.

RIEGL Laser Instrument Systems, 2013, RIEGL VZ-400 Technical Documentation and Users Instructions.

Rimmer, S. M., 2004, Geochemical paleoredox indicators in Devonian–Mississippian black shales, central Appalachian Basin (USA). Chemical Geology, 206(3-4), 373-391.

Riquier, L., Tribovillard, N., Averbuch, O., Joachimski, M. M., Racki, G., Devleeschouwer, X., & Riboulleau, A., 2005, Productivity and bottom water redox conditions at the Frasnian-Famennian boundary on both sides of the Eovariscan Belt: constraints from trace-element geochemistry Developments in Palaeontology and Stratigraphy (Vol. 20, pp. 199-224): Elsevier.

Rohlf, F. V. and Robert R. Sokal., 1969, Statistical Sables, W. H. Freeman and Co. 253 pp.

Rush, J., & Kerans, C., 2010, Stratigraphic response across a structurally dynamic shelf: the latest Guadalupian composite sequence at Walnut Canyon, New Mexico, USA. Journal of Sedimentary Research, 80(9), 808-828.

Sarg, J., 1988, Carbonate sequence stratigraphy.

Sluijs, A., Röhl, U., Schouten, S., Brumsack, H. J., Sangiorgi, F., Sinninghe Damsté, J. S., & Brinkhuis, H., 2008, Arctic late Paleocene–early Eocene paleoenvironments with special emphasis on the Paleocene-Eocene thermal maximum (Lomonosov Ridge, Integrated Ocean Drilling Program Expedition 302). Paleoceanography, 23(1).

Sturdivant, S. K., Díaz, R. J., & Cutter, G. R., 2012, Bioturbation in a declining oxygen environment, in situ observations from Wormcam. PloS one, 7(4), e34539.

Taylor, S., & McLennan, S., 1985, The continental crust: Its evolution and composition. Lon on: Blackwell.

Thermo Fisher Scientific, 2010, User's Guide Version 7.1

Tinker, S. W., 1998, Shelf-to-basin facies distributions and sequence stratigraphy of a steep-rimmed carbonate margin: Capitan depositional system, McKittrick Canyon, New Mexico and Texas. Journal of Sedimentary Research, 68(6).

Tréanton, J.A. 2014. Outcrop-derived chemostratigraphy of the Woodford Shale, Murray County, Oklahoma. M.S. thesis, The University of Oklahoma. 83pp.

Tribovillard, N., Algeo, T., Baudin, F., & Riboulleau, A., 2012, Analysis of marine environmental conditions based onmolybdenum–uranium covariation—Applications to Mesozoic paleoceanography. Chemical Geology, 324, 46-58.

Tribovillard, N., Algeo, T. J., Lyons, T., & Riboulleau, A., 2006, Trace metals as paleoredox and paleoproductivity proxies: an update. Chemical Geology, 232(1-2), 12-32.

Turner, B., 2016, Utilization of chemostratigraphic proxies for generating and refining sequence stratigraphic frameworks in mudrocks and shales.

Tyson, R. V., & Pearson, T. H., 1991, Modern and ancient continental shelf anoxia: an overview. Geological Society, London, Special Publications, 58(1), 1-24.

van Buchem, F. S., Pittet, B., Hillgarten, H., Grotsch, J., Al-Mansouri, A., Billing, I., Van Steenwinkel, M., 2002, High-resolution sequence stratigraphic architecture of the Barremian-Aptian carbonate systems in northern Oman and the United Arab

Emirates Kharaib and Shu'aiba Formations. GEOARABIA-MANAMA-, 7, 461-500.

Van Wagoner, J. C., 1995, Sequence stratigraphy and marine to nonmarine facies architecture of foreland basin strata, Book Cliffs, Utah, USA.

Wedepohl, K., 1971, Environmental influences on the chemical composition of shales and clays. Physics and Chemistry of the Earth, 8, 307-333.

Wedepohl, K., Heinrichs, H., & Bridgwater, D., 1991, Chemical characteristics and genesis of the quartz-feldspathic rocks in the Archean crust of Greenland. Contributions to Mineralogy and Petrology, 107(2), 163-179.

Wilde, P., Lyons, T. W., & Quinby-Hunt, M. S., 2004, Organic carbon proxies in black shales: molybdenum. Chemical Geology, 206(3-4), 167-176.

Williams, Michael T., John D. Pigott, and Kulwadee L. Pigott, 2014, Delaware Basin Evolution: Preliminary Integrated 1D,2D, And 3D Basin Model for Petroleum System Analysis, 2014, AAPG Annual Convention & Exhibition, Houston, Tx.

Yarincik, K., Murray, R., & Peterson, L., 2000, Climatically sensitive eolian and hemipelagic deposition in the Cariaco Basin, Venezuela, over the past 578,000 years: Results from Al/Ti and K/Al. Paleoceanography, 15(2), 210-228.

Zhou, Y., 2014, High resulution spectral gamma ray sequence stratigraphy of shelf edge to basin floor Upper Capitan Permian carbonates, Guadalupe Mountains, Texas and Delaware Basin, New Mexico. Master's Thesis, University of Oklahoma, 143.

Appendix A: Preliminary XRF measurements before washing and after washing

Index+AA10:BX11	1	4	Index+AA10:BX11	1	4
Reading No	8	11	Reading No	8	11
Type	TestAll Geo	TestAll Geo	Type	TestAll Geo	TestAll Geo
Duration	222.27	222.44	Duration	222.27	222.44
Units	ppm	ppm	Units	ppm	ppm
Sigma Value	2	2	Sigma Value	2	2
Sequence	Final	Final	Sequence	Final	Final
Flags	-3mm	-3mm	Flags	-3mm	-3mm
SAMPLE	Before Washing	After Washing	SAMPLE	Before Washing	After Washing
Ba	252.79	204.82	Cu	106.98	118.08
Ba Error	35.57	35.95	Cu Error	11.5	12
Sb	< LOD	< LOD	Re	< LOD	< LOD
Sb Error	13.6	13.93	Re Error	1.5	1.5
Sn	25.03	< LOD	Ta	< LOD	< LOD
Sn Error	10.41	22.94	Ta Error	1.5	1.5
Cd	< LOD	< LOD	Hf	< LOD	< LOD
Cd Error	6.46	6.85	Hf Error	1.5	1.5
Pd	< LOD	< LOD	Ni	< LOD	< LOD
Pd Error	2.97	2.9	Ni Error	39.17	40.17
Ag	< LOD	< LOD	Co	43.75	< LOD
Ag Error	6.37	4.93	Co Error	24.4	36
Bal	682144.6	663617.2	Fe	2557.24	2284.56
Bal Error	1133.6	1231.75	Fe Error	71.27	69.55
Mo	< LOD	< LOD	Mn	224.33	320.07
Mo Error	2.25	2.21	Mn Error	56.46	59.47
Nb	3.75	4.32	Cr	< LOD	< LOD

Nb Error	1.22	1.25	Cr Error	50.61	35.97
Zr	12.46	10.63	V	< LOD	< LOD
Zr Error	1.66	1.68	V Error	30.82	29.93
Sr	128.26	128.82	Ti	363.93	369.57
Sr Error	2.85	2.92	Ti Error	63.34	64.57
Rb	3.29	3.04	Ca	302699.3	310784.9
Rb Error	1	1	Ca Error	1415.72	1459.01
Bi	9.81	7.23	K	154.39	152.53
Bi Error	3.64	3.63	K Error	185.15	145.01
As	< LOD	< LOD	Al	1756.2	1820.58
As Error	4.81	5.76	Al Error	1052.83	803.99
Se	< LOD	< LOD	P	231.02	216.42
Se Error	6.4	5.53	P Error	214.51	122.23
Au	< LOD	< LOD	Si	9343.94	7847.51
Au Error	7.96	8.35	Si Error	381.8	358.84
Pb	< LOD	6.97	Cl	732.22	790.24
Pb Error	5.09	3.51	Cl Error	41.5	42.94
W	175.17	198	S	850.18	865.64
W Error	32.5	34.03	S Error	84.69	86.05
Zn	98.26	101.06	Mg	9768.02	9974.04
Zn Error	9.31	9.64	Mg Error	6924.8	6098.7